Characterization of a Rotating Gliding Arc in Argon at Atmospheric Pressure

Mitchell McNall

Department of Chemical Engineering

McGill University

Montréal, Québec, Canada

April 2018

Supervisor: Professor Sylvain Coulombe

A thesis submitted to McGill University
in partial fulfillment of the requirements
of the degree of Master of Engineering.

Acknowledgement

I would like to thank my supervisor Professor Sylvain Coulombe for his continued support throughout my Master's thesis. He pushed me to pursue a project that was of great interest to me and without his advice and guidance it would not have been possible. Through his example I have gained valuable experience in conducting research.

This project would have not run as smoothly if it weren't for my colleagues. Felipe and Mathew were always around when I had questions and were able to push me in the right direction and I am extremely grateful for their help. Daniel worked on a similar image analysis technique, and his shortest length algorithm helped with obtaining results for this thesis. A special thanks goes out to the whole PPL group; Felipe, Larissa, Adya, Daniel, Cristina, Pablo, Mathew, Kathryn, Evelyne, Pierre-Alexandre and Dominic for being good friends throughout.

I would also like to thank Professor Anne-Marie Kietzig for allowing me to use the high-speed camera for my experiments. Without the camera most of the results in this thesis would not have surfaced.

I would also like to extend my thanks to the technical and administrative staff without whom this project would not have been possible. An extra special thanks goes to Gerald, Lou and Frank, who also became good friends too chat with in the office.

Funding for this project helped me live in the city of Montreal to complete this study. I would like to acknowledge the financial support from the Eugenie Ulmer Lamothe funds, the Gerald Hatch Faculty Fellowship, and NSERC.

Lastly, my family and friends have been there for me throughout the entire thesis. Mom, dad and Jenna I couldn't have done this without your support through the good and the bad portions of this project. Visits and weekend trips with you guys gave me the motivation to get through it.

Abstract

With a growing desire for environmentally friendly processes, gliding arc technology has become an appealing solution as it uses electricity to produce a highly reactive medium. These simple, inexpensive devices produce a non-thermal plasma at atmospheric pressure with high electron temperatures and moderate gas temperatures. In this work we develop a rotating gliding arc operated with argon to study the electrical and physical characteristics of the rapidly moving arcs. High-speed imaging and electrical diagnostics are used to gain an understanding of the projected arc length, position of the arc attachment spot on the central cathode, and frequency of arc rotation. With the settings in this study, the device draws a low amount of power (~40 W) and can be operated in two different modes. Restrike mode, where traditional gliding arcs are observed, and when the applied voltage is increased a disc mode, where the arc becomes diffuse and immobile, and no longer restrikes. Increased turbulence and drag force on the arcs at higher flow rates causes the discharge to re-strike more frequently. This causes the arc to stay confined near the base of the cone and keeps the average projected arc length low. The square root dependency of the arcs rotation frequency on the applied current predicted by a simplified model considering the gas vortex drag and Lorentz forces is confirmed with measurements. A proportionality constant comprising variables based on the device and operating regimes was measured and falls within the predicted limits. High rotation frequencies are achieved (~100-300 Hz) with average projected arc lengths of 4-8 mm creating a large reactive volume. Our observations delineate trade-offs for the further optimization of this device for gas processing. One would intuitively believe that increasing that vortex gas flow rate allows to elongate the arcs and enhance the processing volume, but the accompanying increase in restrike frequency counteracts this action.

Abrégé

Dernièrement, l'industrie chimique a vu une demande croissante pour la modification des procédés chimiques afin de minimiser les impacts environnementaux. La technologie de l'arc glissant représente une solution simple et peu coûteuse, capable de soutenir un milieu très réactif à partir d'un courant électrique et un gaz porteur. Lorsque ce type d'arc est opéré à la pression atmosphérique, un plasma non-thermique est produit. Il s'agit d'un environnement réactif contenant un gaz d'électrons à haute température et un gaz de particules lourdes à température modérée. Ce mémoire de maîtrise porte sur le développement d'un arc glissant rotatif utilisant l'argon comme gaz porteur et une étude préliminaire de ses caractéristiques électriques et physiques. L'imagerie à haute vitesse et plusieurs autres diagnostics électriques ont été effectués afin d'étudier la longueur d'arc projetée, la position du point d'ancrage de l'arc sur la cathode centrale et la fréquence de rotation de l'arc. Le dispositif opère à une puissance de ~40 W pour les conditions expérimentales décrites. Deux modes de déplacement de l'arc sont observés : Le premier est un mode de réamorçage communément observé avec les arcs glissants où l'arc se déplace par une succession de sauts. Le deuxième mode d'opération est observée à tension élevée. L'arc est alors diffus et immobile, sans réamorçage. L'augmentation du débit de gaz entraîne une perte de stabilité et des réamorçages plus fréquents, causés par une turbulence plus importante et une force de traînée plus grande sur l'arc glissant. Un modèle simplifié considérant la force de traînée causée par le vortex de gaz et la force de Lorentz prédit que la fréquence de rotation de l'arc varie selon la racine carrée du courant appliqué. Cette prédiction est confirmée avec les mesures électriques. La valeur de la constante de proportionnalité du modèle obtenue à partir des mesures expérimentales est dans la gamme prédite avec l'aide des ordres de grandeur des paramètres du dispositif. Des fréquences de rotation élevées ont été observées (~ 100-300 Hz) avec des longueurs moyennes d'arc projetées de 4-8 mm, créant un grand volume réactif et stable. Nos observations délimitent les compromis requis pour l'optimisation de ce dispositif pour le traitement de gaz. On pourrait intuitivement croire que l'augmentation de la vitesse d'écoulement du vortex de gaz permet d'allonger les arcs et d'augmenter le volume de traitement, mais celui-ci cause une perte de stabilité et des réamorçages plus fréquents, ce qui contrecarre l'avantage des arcs plus longs.

Table of Contents

Acknowledgement ii

Abstract iii

Abrégé iv

Table of Contents v

List of Figures vii

Nomenclature x

Latin Symbols x

Greek Symbols xi

Constants xi

Subscripts xii

Chapter 1. Introduction 1

1.1. Introduction 1

1.2. Objectives 2

Chapter 2. Background & Theory 3

2.1. Plasma Physics 3

2.1.1. Charged Particles 3

2.1.2. Elementary Processes 5

2.1.3. Plasma Statistics 8

2.1.4. Breakdown Phenomena 9

2.2. Arc Discharges 12

2.2.1. Gliding Arc Discharges 15

2.2.2. Modified Gliding Arc Configurations 21

2.2.3. Forces Acting on the Rotating Gliding Arc 30

Chapter 3. Experimental 35
3.1. Rotating Gliding Arc Device 35
3.2. Rotating Gliding Arc Power Supply 36
3.2.1. Cockcroft-Walton Voltage Multiplier 37
3.2.2. Series RC Circuit 40
3.2.3. Circuit Used in this Study 42
3.3. Experimental Set-up 43
3.4. Image Analysis Technique 44
Chapter 4. Results and Discussion 48
4.1. Electrical Analysis 48
4.2. Arc Motion Analysis 52
Chapter 5. Conclusions 61
References 62

List of Figures

Figure 1. Paschen curves for common plasma gasses. Taken from *Principles of Plasma Discharges and Materials Processing, 2nd Edition* [21]. 11
Figure 2. Typical DC circuit used to sustain a gliding arc adapted from Fridman et al [20]. 17
Figure 3. High-speed images of thermal gliding arc discharge, frames separated by 20 ms (left) and typical voltage-current waveforms obtained from the discharge (right). Taken from Mutaf-Yardimci et al. [22]. 20
Figure 4. Voltage vs. arc length curves used to find the electric field of a thermal gliding arc (left) and gliding arc experiencing a transition in equilibrium (right). Taken from Mutaf-Yardimci et al. [22]. 21
Figure 5. Photograph of six knife shaped gliding arc assembly taken from Baba et al. [23]. 22
Figure 6. Voltage characteristic of the 6-phase gliding arc assembly. Taken from Baba et al. [23] 22
Figure 7. Photograph of the reverse vortex gliding arc plasmatron (left) and schematic drawing of the internal structure (right) developed by the Plasmant research group and taken from Ramakers et al. [6]. 23
Figure 8. Schematic of the MSGAD setup: 1 - high-voltage cathode, 2 - grounded anode, 3 - wire attached to cathode, 4 - ceramic ring magnets, 5 - top view of discharge. This schematic was taken from Gangoli et al. [2]. 24
Figure 9. Voltage-current characteristic of the MSGAD at various flow rates. Taken from Gangoli et al. [2]. 25
Figure 10. Schematic of a RGA setup used in this thesis. 26
Figure 11. Schematic of rotating gliding arc and vortex gas ring injector used to enhance combustion. Taken from Wu et. al. [9]. 27
Figure 12. Schematic of rotating gliding arc with tangential inlets directly on cylindrical anode. Taken from Zhang et al. [4]. 28
Figure 13. Voltage and current waveforms at a gas flow rate of 8.3 SLPM with nitrogen (left) and air (right) as the carrier gas. Taken from Zhang et al. [4]. 29
Figure 14. Voltage and current waveforms of a methane-nitrogen mixture at a flow rate of 12 SLPM. Taken from Zhang et al. [28]. 29

Figure 15. Face-down schematic of the coaxial cathode-anode assembly used in this thesis and the forces acting on the gliding arc column. 31
Figure 16. Frequency of arc rotation versus current for the MSGAD taken from Gangoli et al. [2]. 32
Figure 17. Physical arc characteristics in the MSGAD. Plasma diameter (left) and plasma length (right) versus applied current at a flow rate of 4 SLPM. Taken from Gangoli et al. [3]. 33
Figure 18. Time evolution of arc motion using a high-speed camera at 5000 frames per second. Discharge ignited in nitrogen, taken from Zhu et al. [18]. 34
Figure 19. Rotating gliding arc set-up. Left: RGA in atmospheric pressure argon. Right: Schematic with characteristic dimensions. 36
Figure 20. Schematic of a 2-Stage negative polarity Cockcroft-Walton voltage multiplier. 38
Figure 21. Schematic of a simple series RC circuit 41
Figure 22. Homemade power supply used to drive the arcs. Cockcroft-Walton generator (top), current-driver RC circuit (bottom). 43
Figure 23. Schematic of the instrumentation. 44
Figure 24. Single frame obtained from the high-speed camera. 46
Figure 25. Discharge voltage (V_D), current (I_D) and power (P_D) signals for trial V_C = -300 V and Q = 8.8 SLPM. 49
Figure 26. Discharge voltage-current characteristic of entire signal (left) and during the arcing phase (right) for the V_C = -300 V and Q = 8.8 SLPM trial. 50
Figure 27. Average gliding arc discharge power (left) and restrike frequency (right) versus current driver output voltage and total argon flow rate. 52
Figure 28. High-speed imaging (2 ms between frames) of RGA in atmospheric pressure argon with V_C = -325 V and Q = 13.1 SLPM. 52
Figure 29. High-speed imaging (20 ms between frames) of RGA in disc mode with V_C = -325 V and Q = 6.6 SLPM. 53
Figure 30. Measured gliding arc discharge voltage (top) displayed with calculated projected arc length (middle) and height of cathode spot (bottom) for three different trials. All trials at a constant V_C = -325 V and total flow rate, Q, of 6.6 (left), 13.1 (middle) and 21.9 (right) SLPM. 54
Figure 31. Average (left) and maximum (right) projected gliding arc length across all operating conditions. Note: Lines are not part of a model but rather used for ease of visualization. 56

Figure 32. Average (left) and maximum (right) height of the cathode spot across all operating conditions. Note: Lines are not part of a model but rather used for ease of visualization. 57
Figure 33. Measured and fitted average gliding arc discharge current (left) and frequency of arc rotation (right) versus current driver output voltage for Q = 0 SLPM..... 58
Figure 34. Gliding arc discharge current (left) and frequency of arc rotation (right) versus current driver voltage for various flow rates. Gliding arc rotation frequency at V_C = -300 V versus total argon flow rate and changing magnetic field direction (bottom). *Negative f_{Rot} means that the gliding arc rotates in the direction opposite to the one imposed by the aerodynamic drag. 60

Nomenclature

Latin Symbols

B	Magnetic field strength	T
C	Capacitance	F
C_d	Drag coefficient	$-$
d	Distance or gap	m
D	Diameter of arc	m
E	Electric field	V/m
E	Energy	$eV\ or\ J$
E/N_0	Reduced electric field	V/m^2
f	Frequency	Hz
F	Force per unit length	N/m
g	Degeneracy level	$-$
I	Current	A
I_i	Ionization potential	eV
j	Current density	A/m^2
k_i	Ionization rate coefficient	m^3/s
l	Length	m
m	Mass	kg
M	Mass of heavy species	kg
n	Number of stages	$-$
N	Number density	m^{-3}
p	Pressure	$atm\ or\ Pa$
P	Power	W
q	Charge	C
Q	Flow rate	$SLPM$
r	Radius	m
R	Resistance	Ω
R_c	Reflection coefficient	$-$
t	Time	s

T	Total time	s
T	Temperature	K
u	Velocity	m/s
V	Voltage	V
W	Work function	eV

Greek Symbols

α	Townsend ionization coefficient	m^{-1}
γ	Secondary ionization Coefficient	$-$
γ_e	Fraction of kinetic energy transferred	$-$
δ	Voltage ripple	$-$
Δ	Difference	$-$
ε	Electron energy	J
ε_F	Fermi energy level	J
λ	Heat transfer coefficient	$W/(m^2K)$
λ_p	Mean free path	m
μ	Mobility	$m^2/(V\ s)$
ν_i	Ionization frequency with respect to one electron	s^{-1}
ξ	Work function correction factor	$-$
ρ	Density	kg/m^3
σ	Electrical conductivity	$\Omega^{-1}m^{-1}$
$\sigma_{A,B}$	Collision cross section	m^2
υ_d	Electron drift velocity	m/s
ϕ	Electrostatic potential	J/C
ω	Dissipated power per unit length	W/m

Constants

A	Townsend parameter for argon	$12\ cm^{-1}\ Torr^{-1}$
B	Townsend parameter for argon	$180\ V\ cm^{-1}\ Torr^{-1}$
e	Electron charge	$-1.602x10^{-19}\ C$

h	Planck constant	$6.626x10^{-34}\ m^2kg/s$
k_B	Boltzmann constant	$1.381x10^{-38}\ J/K$
m_e	Mass of electron	$9.109x10^{-31}\ kg$

Subscripts

0	Ground state or initial
a	Neutral species
a	Arc
A	Particle A
avg	Average
B	Particle B
C	Current driver
C	Cathode spot
$crit$	Critical
CW	Cockcroft-Walton
D	Drag
D	Discharge
e	Electron(s)
g	Ground state
i	Ion(s) or ionization
j	Elevated "j" state
L	Lorentz
m	Middle
n	Stage number
o	Open load
Res	Restrike
Rot	Rotation
T	Translational
V	Vibrational

Chapter 1. Introduction

1.1. Introduction

Recent work in plasma generation has been majorly focused on atmospheric pressure discharges. One type of plasma source that has been extensively studied is the gliding arc (GA) which shows characteristics of both thermal and non-thermal discharges. Gliding arc systems have been studied mainly for the treatment of pollutant gases [1-7] and assisted combustion [8,9], but also for the degradation of pollutants present in liquids [10-12], and in other applications such as sterilization [13]. Gliding arc discharges have the advantages of low electrode degradation, moderate translational temperatures (800-2100 K) and vibrational temperatures (2000-3000 K), and electron temperatures near 10000 K [14-16]. The simple geometry of the device as well as the use of simple and inexpensive power supplies add to the appeal of these systems. The power supplies used to sustain gliding arc discharges operate in both AC and DC configurations, however DC is the most common. A high-voltage power supply is required to provide a high enough voltage for the breakdown of the gas to occur (~10 kV), and a ballast resistor connected in series is typically used to limit the amount of current. The ballast resistor is typically in the 1-100 kΩ range. Laboratory scale gliding arc systems range in power from 40 to 200 W [1-7] while kW level is used at the pilot scale [17].

Various geometries have been used for the GA anode-cathode assembly, providing both ease of arc ignition and electrical/gas dynamic stabilization. The simplest GA configuration consists of two knife-shaped electrodes that diverge from one another. When an electric field is applied across the gap in the presence of a gas, an arc ignites at the shortest inter-electrode distance. With an aiding gas flow, the arc is elongated and pushed downstream where the inter-electrode gap is larger. The initial arc is thermal in nature, but the moderate gas flow rapidly cools the gas and allows the arc to elongate. Eventually, the arc extinguishes when the power supply voltage becomes insufficient to sustain the discharge, and a new arc re-ignites at the lower inter-electrode gap and the process repeats. This simple geometry offers short residence times and inhomogeneous reactivity [14]. Another geometry produces GAs between a conical electrode surrounded by a hollow cylindrical electrode originally developed by Gangoli et al. [2]. This set-up can operate in

both polarities; however, the inner electrode is usually the cathode while the outer electrode is the anode [4,5,12,18]. With the use of a moderate vortex gas flow and a sufficiently high voltage, successive arcs ignite at the shortest gap and elongate up and around the cone. Using the Lorentz force provided by an external magnetic field, the angular rotation of the GAs can be further enhanced and controlled. Rotating gliding arc (RGA) reactors share similar benefits with traditional ones, with larger and more uniform active volumes providing longer residence times for reactions to take place. The benefits of this technology have been extensively studied, however the dynamics of such RGAs hasn't been characterized at the same level. Richard et al. [19] studied the physical mechanisms of a diverging knife shaped electrode gliding arc system while Gangoli et al. [2] only briefly discussed the RGA dynamics. Recently, Zhu et al. characterized the rotation dynamics of gliding arcs in atmospheric pressure nitrogen and driven by the combined action of a gas vortex and a static external magnetic field [18]. They determined that for their experimental conditions, the external magnetic field plays a dominant role in the stabilization of the arc column and aids in increasing the rotation frequency. The present study aims to provide further insight on the dynamics of RGAs sustained between a conical cathode and a straight tubular anode driven by a combined vortex flow of atmospheric pressure argon and a static external magnetic field.

1.2. Objectives

The main objective of this project is to develop a rotating gliding arc device and supplementary power supply, then to characterize the arc motion and electrical signals. The device must be able to sustain a stable train of gliding arcs for long durations of times. Then, characterization of the different modes that the device can operate in, to gain understanding of the specific device. Power levels and restrike frequencies will be determined across the range of operating conditions. The arc motion will also be characterized using high-speed imaging. Aspects of the arc, such as arc length and height of the arc will be determined through image analysis techniques. Lastly, the forces acting on the arc column caused by the aerodynamic drag, and the magnetic Lorentz force will be studied through frequency of rotation analysis. The goal is to gain a deeper understanding of the arc dynamics in a rotating gliding arc to be able to tune future devices for increased reactivity.

Chapter 2. Background & Theory

2.1. Plasma Physics

Plasma being the fourth state of matter is a highly complex medium with various chemical reactions occurring simultaneously and many different species adding to the complexity. Charged particles as well as its liquid-like properties create matter affected by electromagnetic forces as well as hydrodynamics. The following chapter introduces some of the basic principles occurring in this state of matter that pertains to this study. Unless otherwise stated, the information in this chapter is referenced from *Plasma Physics and Engineering* [20].

2.1.1. Charged Particles

The basic definition of a plasma is that it is an ionized medium consisting of electrons, ions and neutral species in varying quantities. Therefore, one of the main processes occurring in plasma is ionization reactions. The most common charged species are electrons and positive ions, which form a plasma that is quasi-neutral, meaning that the overall bulk of the plasma is charge neutral. In a plasma there can be regions of greater charge density, however the entire body is neutral. When atoms or molecules with a high electron affinity, such as O_2, Cl_2, or SF_6 are used as the plasma forming gas, electrons can combine with the neutral molecule causing negative ion formation.

Arguably the most important species in plasma are the electrons. These are the lightest species in the medium being on average orders of magnitude lighter than ions or neutrals. When an electric field is applied across a gap of gas, the electrons having the smallest mass receive increased energy first. Collisions are the main process by which energy exchange occurs in a plasma, more specifically collisions with electrons that have gained sufficient energy from the electric field. When looking at a plasma there is no single electron energy, but rather a statistical distribution that depends mostly on the electron temperature T_e. The energy distribution $f(\varepsilon)$, can typically be found with the Maxwell-Boltzman distribution function, where k_B is the Boltzman constant as follows:

$$f(\varepsilon) = 2\sqrt{\frac{\varepsilon}{\pi(k_B T_e)^3}}\exp\left(\frac{-\varepsilon}{k_B T_e}\right) \quad (1)$$

The thermal energy gained due to the electric field can be related to the mean kinetic energy in the following way, where m_e is the mass of an electron, and u is the velocity.

$$\langle\varepsilon\rangle = \left\langle\frac{1}{2}m_e u^2\right\rangle = \int_0^\infty \varepsilon f(\varepsilon)d\varepsilon \ = \frac{3}{2}k_B T_e \quad (2)$$

Positive ions are another important species in a plasma. They are the most common ions and are formed when an electron with sufficient energy collides with neutral atoms or molecules, ionizing it, producing a positive ion and another free electron. Due to their heavy mass, ions are only slightly affected by the electric field, and increased energy levels are obtained through collisions with other plasma species. The average kinetic energy of ions is found using the Maxwell-Boltzman distribution similarly to the electrons using equation 1 with the ion temperature. The ion temperature T_i is quite close to the neutral gas temperature T_0 in most cases due too their similar masses. For a neutral atom or molecule to become ionized, an electron must collide with a certain amount of energy. The ionization energy E_i, is quite high. Subsequent ionizations can occur to ions, where another electron is stripped from an already ionized molecule or atom, however this only occurs in plasmas with thermal energies typically greater than 10000 K and is not discussed in this study. This study focusses mainly on plasma generated in argon, so the following reaction is what is expected when ionization occurs.

$$Ar + e^- \ = \ Ar^+ + e^- + e^- \qquad E_i = 15.8\ eV \quad (3)$$

The last key charged species are negative ions. These are formed by collisions, but in this case electrons attach to neutral atoms or molecules. Due to high repulsion effects multi-charged negative ions cannot be produced through electron-ion collisions. The energy distribution follows the Maxwell-Boltzman described in equation 1, again with the ion temperature. Instead of ionization energies, negative ions release energy when they are created and described by their electron affinities. The energy level is much lower than their positive ion counterparts $(0 - 7\ eV)$.

2.1.2. Elementary Processes

Reactions in plasmas are dominated by collisions in which energy transfer occurs. There are two types of collisions that can occur, elastic and inelastic collisions. Two variables used in the determination of any collision to occur are the collisional cross section and the mean free path. The collisional cross section is an assumption made in which two particles whose centroid cross paths causes a collision. Assuming a hard sphere model for particles the collisional cross section $\sigma_{A,B}$ can be found with the radii of two different particles, r_A & r_B.

$$\sigma_{A,B} = \pi(r_A + r_B)^2 \tag{4}$$

The mean free path λ_p shows the distance required for a particle to travel before a collision to occur by relating the collisional cross section and the number density (concentration) N_B of a certain type of particle. Therefore, the following equations shows the length particle A must travel in space before colliding with particle B.

$$\lambda_p = \frac{1}{N_B \sigma} \tag{5}$$

When an elastic collision occurs, all kinetic energy is conserved, being transferred from one species to another. The internal energy of the species does not change and does not result in the change of chemical composition or excitation level. These collisions therefore play little role in the reactivity of the plasma, however have an effect on the conductivity and drift/diffusion. Since kinetic energy is conserved the following equation shows the fraction of energy transferred γ_e from one molecule of mass m to another molecule of mass M.

$$\gamma_e = \frac{2mM}{(m+M)^2} \tag{6}$$

Therefore, it is quite apparent that an elastic collision between an electron and a heavy particle only transfers a small fraction of kinetic energy ($\gamma_e \sim 10^{-4}$).

Inelastic collisions drive the chemical reactions that take place in a plasma. Ionization, ion-ion recombination, excitation, relaxation and dissociation are all elementary processes that can take place when an inelastic collision occurs in a certain way.

2.1.2.1. Ionization

Ionization is the most important process that takes place in a plasma, as it is what generates the charged species involved. The first and simplest ionization process that occurs is direct electron-neutral ionization. Here, when an electron has sufficiently high energy, greater than the ionization energy of the neutral, a direct ionization occurs. These ionizations are most apparent in non-thermal plasmas, plasmas where the electrons are at a much higher energy level than the heavy particles. This type of plasma is generally formed at low pressures and when a high electric field is applied electrons commonly reach high energy levels before collision. This causes a medium with a low amount of excitations and a large amount of direct ionizations.

Another type of ionization occurs more frequently in thermal plasmas, plasmas in which the electron energy is close to that of the heavy species. In this case inelastic collisions where excitations occur (particles moving up in potential energy levels) are more frequent. Eventually, an electron collides with an excited molecule causing ionization to occur, however in a step-wise manner.

2.1.2.2. Electron Losses

Another elementary process that occurs in plasmas are reactions that consume free electrons and reduce the reactivity of the plasma. The reactions that consume free electrons are highly exothermic, and the excess energy released is consumed by another process simultaneously.

Three body electron-ion recombination is a process that occurs mostly in atomic plasma, with low concentrations of molecular gas. This study focusses on atomic argon plasma, so this is the most prominent loss of electrons. This process is essentially the reverse of stepwise ionization discussed in the previous section. Two electrons and a positive atom recombine causing the atom to neutralize and become highly excited and the remaining free electron gains significant kinetic energy. Further collisions with low energy electrons continue to relax the ion, followed by a final relaxation, which is a radiative relaxation down to the ground state.

Another electron loss mechanism occurring in plasma is radiative electron-ion recombination. When an electron collides with an ionized atom predominantly in low density

plasmas, the particles recombine, causing the atom to enter an elevated excitation state. The large amount of exothermic energy is then expelled as a photon at a certain wavelength.

2.1.2.3. Excitation

The last phenomena occurring in a plasma is excitation and de-excitation of atoms and molecules. There are three types of excited species that can exist such as electronically excited, rotationally or vibrationally excited species. The main focus of this study does not look specifically at excited species, however they are quite important states since majority of the energy put into the production of a plasma goes into vibrationally exciting species.

To fully understand what is meant by excitation a brief introduction to quantum mechanics is required. Any atom that is at its lowest stable energy state is considered to be at a ground level of potential energy. If the atom gains some form of energy, through absorption, or in the case of a plasma via electron impact, the potential energy of the species increases. More specifically, one of the electrons in the outer orbit is affected by the energy change, causing it to change orbit or angular momentum. This electronically excited atom stays in this state for an amount of time dependent on the type of atom and state it entered (usually about $10^{-8} – 10^{-6}$ s). Eventually, the electron returns back to the ground level and when this occurs a photon with a wavelength proportional to the amount of potential energy change is released and is called radiative transition. Through quantum mechanics a set of rules are defined for when and how de-excitation can occur. Some excited species cannot undergo radiative transition because they enter a stable excited state, and the lifetime of these species can be much longer. These species are called metastable excited states and for the case of argon there is a range of lifetimes up to 40 s. Due to the extended lifetime, these species play a major role in the chemical reactions occurring in the plasma. Collisions with metastables can cause a variety of reactions. The elevated energy level allows the excited species to be ionized with lower energy electron collisions. Radiative transition can occur with these species, but they may also undergo collisional relaxation processes.

2.1.3. Plasma Thermodynamics

The definition of temperature in plasma is not simple. In a completely ideal scenario a plasma at complete thermodynamic equilibrium (CTE) can be used to define the reactions and kinetics occurring in the bulk of the plasma. In most plasmas this is not a realistic possibility. The closest definition is a plasma at local thermal equilibrium (LTE). Here, it is assumed that energy exchange is dominated by collisions and that energy exchange through radiation is negligible. Therefore by assuming a plasma is at LTE allows it to be described by one temperature that comes from collisional energy exchange and is different than Plank's radiation temperature. A thermal plasma is a plasma to be assumed to be in LTE, where the temperature or kinetic energy of the heavy species is the same as the electrons. This type of plasma requires a high degree of current density to sustain and a large portion of the applied energy goes into thermal processes. Non-thermal plasmas, or plasmas that deviate from LTE have two different temperatures involved. The electrons have a much higher kinetic energy than the heavy species and causes collision-based reactions to be the main use of the applied energy, with less used for gas heating. This two-temperature concept complicates any equilibrium calculations that can be made since they are all a function of temperature.

Various statistical distributions of equilibrium can be found defined by the temperature. The first one that was discussed previously is the Maxwell-Boltzman kinetic energy distribution. Most of the species in a plasma can also be statistically determined using a temperature.

The number density of excited species can be determined through the Boltzman distribution. Here, the subscripts j and g define the state, either an elevated or ground state respectively. N denotes the number density, E is the energy required to reach the elevated state, T is the temperature and g is the statistical weight of the state occurring.

$$N_j = N_g \frac{g_j}{g_g} \exp\left(-\frac{E_j}{k_B T}\right) \tag{7}$$

The Saha Equation is used to describe the ionization equilibrium, linking the number densities of neutrals, ions and electrons. In this equation h is Planck's constant. The subscripts e, i and a denote electrons, ions and neutrals respectively.

$$\frac{N_e N_i}{N_a} = \frac{g_e g_i}{g_a}\left(\frac{2\pi m_e k_B T}{h^2}\right)^{\frac{3}{2}} \exp\left(-\frac{E_i}{k_B T}\right) \tag{8}$$

The distribution function of dissociation equilibrium and radiative equilibrium can also be found in a similar equation based on temperature.

2.1.4. Breakdown Phenomena

Electrical breakdown of a gas occurs when an electric field threshold is surpassed, and a non-conducting gas becomes conductive, producing a plasma. Generally, breakdown occurs quickly (0.01 – 100 μs) and starts with an electron avalanche. When a sufficiently large electric field is applied across two electrodes separated by a distance d, free electrons accelerate from near the cathode to the anode. The electrons collide with and ionize neutrals, subsequently producing more free electrons. This causes a cascading effect where more and more ionizations occur along the length of the electric field.

To quantify the electron avalanche two terms are used. The primary Townsend ionization coefficient α, shows the number of electrons produced per length (in the electric field direction).

$$\alpha = \frac{\nu_i}{v_d} = \frac{1}{v_d} k_i \left(\frac{E}{N_0}\right) N_0 = \frac{1}{\mu_e} \frac{k_i \left(E/N_0\right)}{E/N_0} \tag{9}$$

Each section of this equation can be broken down. The primary Townsend ionization coefficient is a measure of the quotient of the ionization frequency with respect to one electron ν_i and the electron drift velocity v_d. The ionization frequency can be simplified into the ionization rate coefficient $k_i(E/N_0)$ multiplied by the number density of initial electrons N_0. The ionization rate coefficient is therefore dependent on the ionization constant k_i, which depends on the gas, and the reduced electric field E/N_0. The drift velocity can then be found as the product of electron mobility μ_e, which is dependent on the pressure of the system, and the electric field. From this equation it is clear that the type of gas used, the pressure and the applied electric field affect the primary Townsend ionization coefficient.

As the electron avalanche is occurring ion number density is simultaneously increasing, and the ions accelerate towards the cathode. The heavy species gain a significant amount of kinetic

energy and bombard the cathode. This high energy impact can eject new free electrons from the surface of the cathode, giving rise to the secondary electron emission coefficient γ. This coefficient is largely dependent on the cathode material. The type and the state of the metal cathode, type of gas and reduced electric field affect this coefficient. For most cathode-gas combinations the secondary emission coefficient ranges between 0.01 and 0.1 and is unitless.

To determine the conditions of breakdown a measure of the current in the gap needs to be found. The Townsend formula describes this and relates the two emission coefficients, the initial electron current I_0 and the gap between the electrodes d.

$$I = \frac{I_0 \exp(\alpha d)}{1 - \gamma[\exp(\alpha d) - 1]} \tag{10}$$

If the denominator in this equation is positive the current in the gap is non-self-sustained, meaning the species in the plasma do not form a sufficient conductive channel. However, as the denominator approaches zero, the current in the gap becomes self-sustained and breakdown occurs. The way this occurs is by increasing the primary Townsend coefficient. Therefore, simple rearrangement of the denominator provides the breakdown criteria of a system.

$$\alpha d = \ln\left(\frac{1}{\gamma} + 1\right) \tag{11}$$

To further simplify the criteria of breakdown, it is convenient to display equation 9 using similarity parameters, α/p and E/p, where p is the pressure. This rearrangement provides two new parameters, A and B, that depend only on the gas being used.

$$\frac{\alpha}{p} = Aexp\left(\frac{B}{E/p}\right) \tag{12}$$

For argon, parameter A is $12\ cm^{-1}\ Torr^{-1}$ and B is $180\ V\ cm^{-1}\ Torr^{-1}$. Substituting equation 12 into equation 11, yields the required voltage for breakdown, dependent on an important parameter, pd $(cm\ Torr)$.

$$V = \frac{B(pd)}{C + \ln(pd)} \tag{13}$$

This equation is known as the Paschen curve equation, where one can find the required voltage for breakdown to occur for specific reactor dimensions and conditions. The parameter C can be found as $C = lnA - \ln\{ln[(1/\gamma) + 1]\}$. Therefore, depending on the gas used, the cathode used, the pressure and the distance between electrodes an approximation of the required voltage for breakdown can be found. It is interesting to note that equation 13 reaches a minimum at a certain value of pd. If the pressure or distance between electrodes is lower, fewer collisions occur, meaning a higher voltage is required to cause an electron avalanche. On the contrary, if the pressure or distance is too high, many collisions occur, however at lower energy levels. To compensate a higher applied voltage is required to cause more ionizing collisions. Paschen curves for various plasma forming gasses can be seen in Figure 1. Typical minimum voltages are around 300 V, however they require low pressures. Since this study focuses on a device operated at atmospheric pressure, and argon as the carrier gas, the minimum electric field to break down the gas would be approximately 10-20 kV/cm.

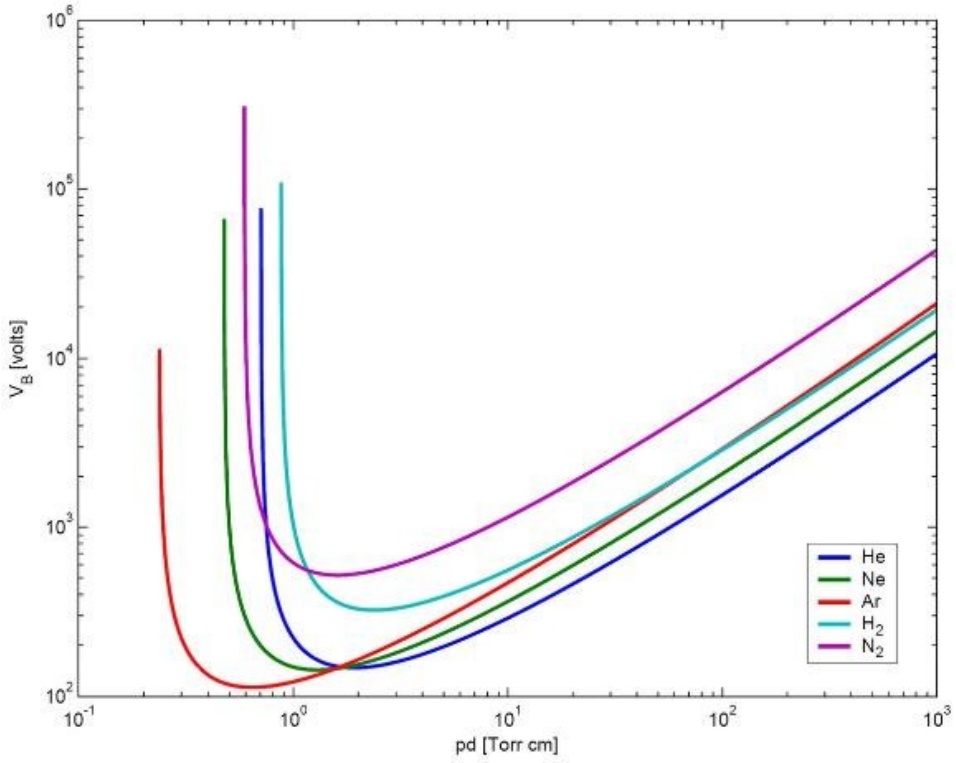

Figure 1. Paschen curves for common plasma gasses. Taken from *Principles of Plasma Discharges and Materials Processing, 2nd Edition* [21].

2.2. Arc Discharges

Arc discharges are unique in that they are typically a confined volume of highly reactive species, in the shape of an arc. Most arc discharges are at local thermal equilibrium (LTE) with high temperatures (>10000 K) and have high current densities. Heat fluxes from the arc cause the cathode and anode to endure high temperatures and require cooling systems to be in place for most cases. Most arc discharges are operated at or around atmospheric pressure. When the pressure is too low the discharge tends to deviate from LTE. Electric arcs are formed from a glow-to-arc transition mechanism, which is typically on the order of microseconds. This transition occurs when the current density is increased past a typical glow level. This causes the cathode to heat up emitting more electrons, allowing a rapid transition to an arc, with a drastic voltage drop and increased current density.

The secondary electron emission coefficient discussed in the previous section holds true for all discharges. However, in arc discharges this is not the only form of secondary electron emission and in most cases electron emission by ionic bombardment is negligible. The main source of electrons is via intense thermionic and field emission from the arc cathode. Gliding arcs are an exception, where all three processes can be occurring at the same time, depending on the discharge current and electric field. The most prominent mechanism of electron emission from the cathode depends mostly on the type of arc discharge. In thermal electric arcs, thermionic emission dominates and if the electric field is high enough a combination of the two, thermo-field emission contributes.

Thermionic emission occurs when a metal surface is heated to a high temperature. Electrons in the metal reach high thermal energies and break free from the metal. The potential energy of the metal needs to be surpassed by the kinetic energy of an electron for one to be emitted. This phenomenon can be described as the saturation current density j, and is a function of the work function $W = -e\phi$ and the temperature. The work function quantifies the amount of energy required for an electron to be extracted from the metal, with e being the electron charge, ϕ the electrostatic potential. The Sommerfeld formula shows this.

$$j = 120\, T^2(1 - R_c) \exp\left(-\frac{W}{k_B T}\right) \tag{14}$$

Here, R_c is the reflection coefficient based on the metal typically either ~0 or ~0.8, and the work function is also related to the type of metal. The unit of the coefficient is A/cm^2K^2. The surface electric field produced by the presence of ions in the cathode region affects the work function of the metal by means of the Schottky effect. This can be shown as a relationship between the work function at no electric field, W_0 and the electric field .

$$W = W_0 - 3.8x10^{-4}\sqrt{E} \tag{15}$$

The unit of the electric field is V/cm. Based on this equation increasing the electric field shows diminishing returns on lowering the work function, and the magnitude of the change in work function is quite small even at reasonable electric fields. However, the exponential dependence the work function has on the saturation current means that the Schottky effect plays a large role in increasing thermionic emission.

At high temperatures and high electric fields, a synergistic effect of field emission and thermionic emission can occur. This is called thermo-field emission and both electron tunnelling and increased electron temperatures in the metal causes increased current densities at the cathode.

An arc discharge can be divided into three separate locations of interest when describing various mechanisms. Arguably the most important is the cathode layer, inside which essential processes are taking place to sustain the discharge. The largest volume is comprised of the positive column, which is the most reactive region and is followed by the anode layer.

Near the cathode a high number density of ions is observed, arising in a net positive space charge. The reason for this is due to the mechanisms by which electrons are emitted from the cathode. In either thermionic or field emission, electrons with a significant amount of kinetic energy are ejected away from the cathode. A large percentage (70-90%) of the electron current in the cathode layer originates from electrons ejected from the cathode. On average less than one generation of electrons is produced by gas phase collisions in the arc, resulting in a small voltage drop observed in the cathode layer. The cathode layer can be separated into two different regions. A very short collisionless boundary directly adjacent to the cathode that is shorter than the mean free path of collision between the electrons and heavy species. Ions in the cathode layer are accelerated towards the cathode, making up most of the species in this collisionless layer. This causes a very high electric field directly adjacent to the cathode, aiding in field emission. After the

collisionless layer, a longer quasineutral layer begins, where the density of electrons approaches that of the ions. In this region, the electrons have gained a significant amount of kinetic energy due to the electric field, and intense ionization reactions begin. The number density of the ions approaches the number density of the electrons as the distance from the cathode increases.

In the positive column the electric field stays relatively constant. Ionizations along the column continue to happen, so a small potential drop is witnessed. The positive column is the highest temperature region of an arc. Heat transfer mechanisms dominate energy exchange from the arc column to the surrounding gas in three different ways. Water cooled walls, flow stabilization, or electrodes can effectively receive the heat from the positive column. In a thermal electric arc, the plasma properties are easily determined, only being a function of the temperature and pressure. The pressure is given based on the operating conditions, so only a temperature distribution is required for modelling a cylindrical arc column. The radial distribution can be described by the Elenbaas-Heller equation, where r is the radius, $\lambda(T)$ is the heat transfer coefficient, and $\sigma(T)$ is the electrical conductivity. This equation assumes that the pressure and current are not too high, and the plasma temperature does not exceed $1\ eV$. Also, radiation is neglected and the heat transfer in the entire arc column is simplified with the heat transfer coefficient.

$$\frac{1}{r}\frac{d}{dr}\left[r\lambda(T)\frac{dT}{dr}\right] + \sigma(T)E^2 = 0 \tag{16}$$

Further analysis of the positive column shows that the radial temperature profile follows a gradual decrease from the center of the arc to the edge. Whereas, the electrical conductivity falls drastically from the center towards the edge. Therefore, a channel model is proposed where the arc current is only apparent in a channel of radius r_0 from the center of the arc (region where electrical conductivity changes). Using this as a basis and assuming the temperature and electrical conductivity to be constant throughout the "channel" an equation can be derived to find the dissipated power per unit length of the arc ω. It is known as the Raizer channel model, where T_m is the maximum value of temperature at the center of the arc column, λ_m is the heat transfer coefficient at the center of the arc, and I_i is the ionization potential of the gas.

$$\omega = 8\pi\lambda_m(T_m)\frac{T_m^2}{I_i} \tag{17}$$

After the positive column, the anode layer is observed and is not fully understood. The positive electrode repels positive ions and develops a negative space charge near the anode, defining the anode layer. This causes an increased electric field, and hence a voltage drop across the layer. The temperature of this region is lower than the positive column due to enhanced heat transfer from the anode. The role of the anode layer is easy to visualize, but the physical mechanisms are not well described and understood yet.

2.2.1. Gliding Arc Discharges

A gliding arc discharge sustains a plasma volume generated between two diverging electrodes with an aiding gas flow at atmospheric pressure or above. Traditionally, two knife shaped electrodes are placed in a vessel as seen in Figure 2, such that there is a short inter-electrode gap of approximately 1-2 mm. When a sufficiently high voltage potential is applied across the gap, an electric arc ignites at the shortest inter-electrode gap, initiating a conductive arc column. The aiding gas flow pushes the arc column downstream, and due to the diverging electrodes, elongates the arc column. Eventually, the required sustaining voltage becomes greater than the maximum that the power supply can provide and the arc extinguishes. A new arc then reignites at the shortest inter-electrode gap and the whole cycle repeats.

Gliding arc devices can be operated as completely thermal at high power levels, or more commonly as a non-thermal discharge. Thermal gliding arcs can range from 1 kW to over 50 MW, however due to the thermal nature of the discharge, plasma chemistry selectivity is quite low, where much of the energy is spent as thermal dissipation. Therefore, low power non-equilibrium gliding arcs are more attractive devices for providing highly reactive species at low–moderate temperatures.

Although gliding arcs mostly deviate from local thermodynamic equilibrium, there are multiple stages in the evolution of the arc. At the shortest inter-electrode gap when breakdown occurs, for a very short period of time the arc is thermal by nature. In a time of ~ 1 μs, a drastic voltage drop occurs across the electrodes and a low resistance conducting channel is formed. Along with a voltage drop a large amount of current is fed into the arc column. While the arc is still short and draws large amounts of current it is in an equilibrium stage. Here, the gas temperature does

not change drastically and typically lies in the range 7000 < T_0< 10000 K, however for low power gliding arcs under 200 W, gas temperatures can be as low as 2500 K. The Elenbaas-Heller equation described in the previous section can be used to obtain an estimation of the temperature distribution for the arc in this phase.

At the same time the gas flow is causing the arc to be pushed downstream. Eventually a critical length of the column is reached, and the plasma starts to deviate from equilibrium. The gas flow is rapidly cooling the arc column and the heat losses exceed the energy input from the power supply. The bulk of the gas cools to below 2000 K, however the plasma is still maintained with high energy electrons T_e ~ 1 eV. The arc continues to elongate, until the required voltage to sustain it reaches the maximum that the power supply can provide, at which point it extinguishes and the process repeats.

A simple DC power supply to sustain a gliding arc consists of two parts as seen in Figure 2. One stage is a high voltage-low current supply, which is used to overcome the breakdown voltage of the gas. The other stage of the power supply requires a higher current, with a lower voltage. Once the conductive channel is initiated by the high voltage supply, this power supply becomes active and provide the current and power needed to sustain the growing arcs. Typically, a ballast resistor is required in series with this power supply to limit the current being fed to the system. More complicated power supplies can be used, such as AC, three-phase, or multiple electrode configurations, but a simple and efficient homemade DC power supply was developed and used in this study.

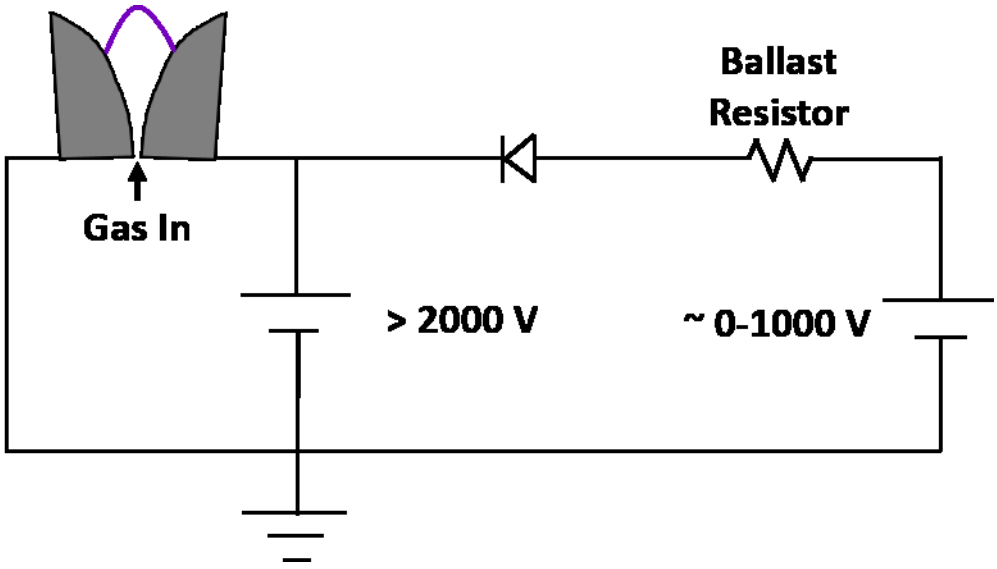

Figure 2. Typical DC circuit used to sustain a gliding arc adapted from Fridman et al [20].

A simple electrical circuit model of the gliding arc can be obtained using Ohm's law, considering the two loads being the ballast resistor and the varying-resistance arc column. Here, the electrical circuit to elongate the arcs is modelled considering the open circuit voltage V_o from the high current power supply. This assumes that the conductive channel is already formed.

$$V_o = RI + \omega \frac{l}{I} \tag{18}$$

The value of the ballast resistor R, discharge current I, arc length l and power dissipated per unit length of the gliding arc ω are used. The power dissipated in the arc channel can be found using the Raizer "channel" model, however in the typical temperature range of gliding arcs, the dissipated power is approximately 50-70 kW/m. Rearranging equation 18 and solving for the current gives the following function.

$$I = \frac{V_o \pm (V_o^2 - 4\omega l R)^{\frac{1}{2}}}{2R} \tag{19}$$

The solution of equation 19 describes a gliding arc in the equilibrium phase of operation. During this time, the Elenbaas-Heller equation shown in equation 16 can be used to describe the energy balance on the arc column. When the current is greater than $I = V_o/2R$ the arc is operating in the stable quasi-equilibrium regime acting similar to a conventional atmospheric pressure arc

discharge. If one assumes the dissipated power of the arc to be a constant value, the evolution of discharge current and other parameters can be described per length of the arc column. At a length of zero, the current is the highest at a value of $I = V_o/R$. As the arc elongates its differential resistance increases in magnitude. However, arcs follow negative V-I characteristics, thus provides a negative resistance to the circuit. Eventually, it reaches a critical length, which describes the length in which the resistance of the arc is that of the ballast resistance, causing the arc to change operating regimes to a non-LTE state. The critical length can be found by setting the square root in equation 19 to zero as follows.

$$l_{crit} = \frac{V_o^2}{4\omega R} \tag{20}$$

Therefore, as the length increases to the critical length the current decreases to a value of $I = V_0/2R$ before entering a non-equilibrium state. Once stability is lost, the heat losses, ωl continue to increase as the arc elongates, however the power supply has already reached the maximum output. The arc can no longer be sustained in thermodynamic equilibrium and the gas temperature rapidly drops, while the electron temperature is maintained at $T_e \approx 1eV$. During the non-equilibrium state the electric field, E increases and causes the electron temperature to slightly increase. Due to the rapid cooling of the discharge, the electron concentration rapidly falls from $n_e \approx 10^{15}\ cm^{-3}$ in the equilibrium state, to $n_e \approx 10^{12}\ cm^{-3}$ in the non-equilibrium state. This causes a drop in electrical conductivity, σ which results in the reduction of the specific discharge power, σE^2. The growth in electric field is not enough to compensate for the reduction in specific discharge power and is the main reason the arc is unstable. Up to 70-80% of the total gliding arc power is dissipated into this non-equilibrium evolution of the arcs. Measurements by Czernichowski et al. determined the electron temperature to be $T_e \approx 10000\ K$, translational temperature $T_T \approx 800 - 2100\ K$ and vibrational temperature $T_V \approx 2000 - 3000\ K$ in the non-equilibrium region of an air gliding arc discharge [15].

Further research has shown that gliding arcs can operate in three different regimes depending on the input power, gas flow rate and blade geometry [22]. With high power and low gas flow rates the discharge can operate in thermal equilibrium throughout. Conversely, with low power and high gas flow rates the discharge can be non-equilibrium throughout. Lastly, with

moderate power and gas flow rates the discharge experiences a transition from equilibrium to non-equilibrium as the electrodes diverge.

Mutaf-Yardimci et al. studied the various operating regimes of gliding arcs, and performed high-speed image analysis of the discharge [22]. In this study they compared the electrical characteristics to the length of the arcs. Figure 3 displays images of the gliding arc evolution captured using a high-speed camera separated by 20 ms in time (left). The flow rate of air in these experiments was quite high, ranging over 0-400 SLPM, and the power could be as high as 10 kW. Typical voltage and current waveforms of the discharge are shown in Figure 3 (right). The breakdown at the shortest inter-electrode gap (varied from 2-5 mm in this study) occurs with a drastic voltage drop and a sharp current rise. As the arc elongates due to the aiding gas flow, the voltage increases to compensate. Simultaneously, with an increase in arc length, there is an increase in differential resistance, causing the current to fall. Eventually, the arc reaches a length in which the power supply can no longer sustain and a new cycle repeats. In this study lengths of the arcs could reach up to 20 cm in thermal discharges. It was found that an increase in gas flow rate increased the restrike frequency (shorter voltage-current period), due to the arcs being forced downstream quicker.

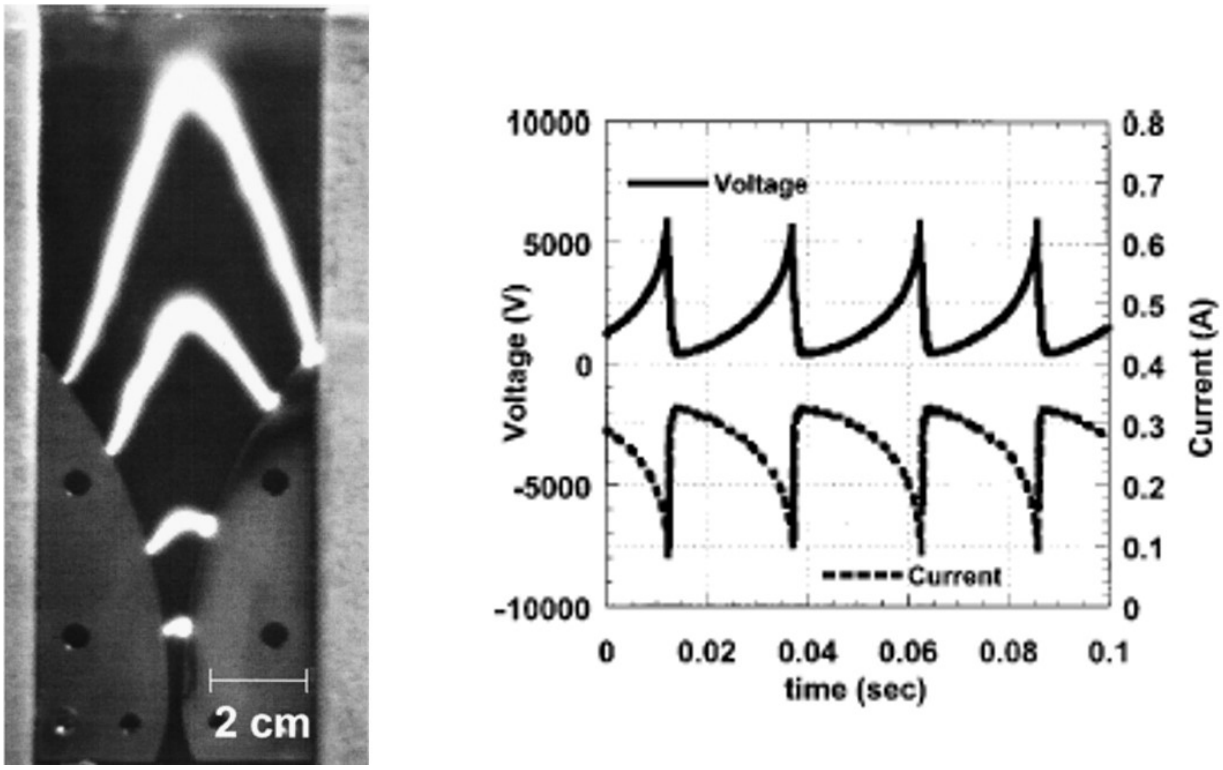

Figure 3. High-speed images of thermal gliding arc discharge, frames separated by 20 ms (left) and typical voltage-current waveforms obtained from the discharge (right). Taken from Mutaf-Yardimci et al. [22].

As previously mentioned the electric field in the positive column of electric arcs is relatively constant throughout. Since the positive column is the main component of a gliding arc, an estimation of the electric field can be found as the slope of a voltage-arc length curve. Figure 4 displays voltage versus arc length curves for a thermal gliding arc (left) and a gliding arc transitioning from equilibrium to non-equilibrium (right). Mutaf-Yardimci et al. found that for gliding arcs operating in equilibrium there was one electric field value across all operating conditions and its magnitude is small [22]. For gliding arcs that transition from equilibrium to non-equilibrium a change in slope is witnessed at the estimated critical length (55 mm in this case) where the electric field increases due to a change in equilibrium.

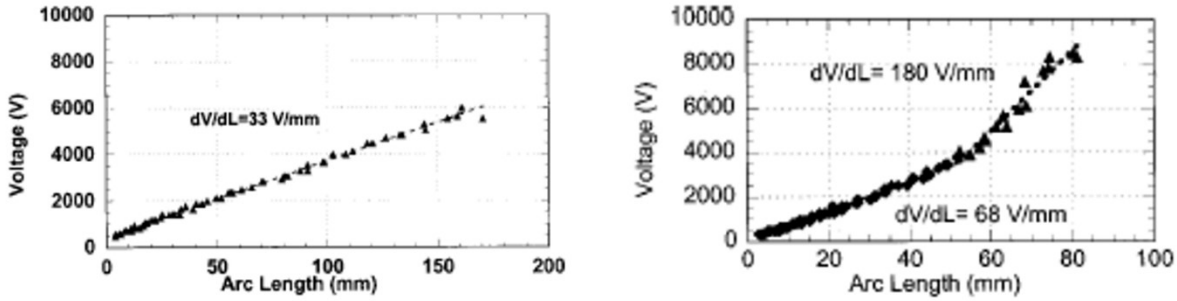

Figure 4. Voltage vs. arc length curves used to find the electric field of a thermal gliding arc (left) and gliding arc experiencing a transition in equilibrium (right). Taken from Mutaf-Yardimci et al. [22].

2.2.2. Modified Gliding Arc Configurations

Recently, the interest in gliding arcs has moved away from the simple diverging knife assembly for various reasons. Amongst the main limitations of the original two-dimensional configuration are low residence times and non-homogenous reactive volumes. Enhanced stabilization can also be achieved using a magnetic field, which is difficult to implement in the traditional configuration.

To increase the reactive volume Baba et al. developed devices with multiple knife shaped electrodes as seen in Figure 5 [23]. Using a three-phase power supply and three electrodes, a three-dimensional reactive volume could be achieved. Even further, with the use of multiple three-phase transformers, a six-phase output could be achieved to ignite a gliding arc between six knife shaped electrodes. This greatly enhanced the homogeneity and volume of a gliding arc. This configuration has a simple geometry, not requiring any special gas injection, however has more complicated power supplies than other gliding arc configurations.

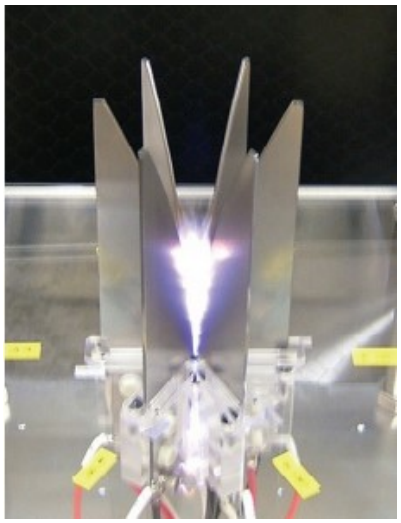

Figure 5. Photograph of six knife shaped gliding arc assembly taken from Baba et al. [23].

Increasing the number of electrodes increased the amount of power that was directed to the discharge region. However, the voltage and current waveforms were quite chaotic and unpredictable. Figure 6 displays the voltage characteristic curve of the system prior to breakdown (0 – 20 ms) and during the discharge (> 20 ms). Argon was used as the operating gas, with a shortest inter-electrode gap of 4 mm.

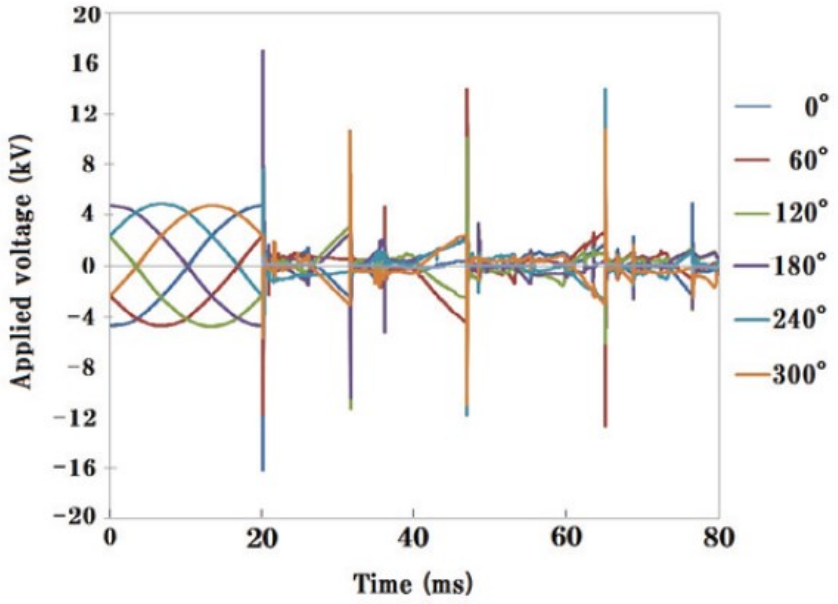

Figure 6. Voltage characteristic of the 6-phase gliding arc assembly. Taken from Baba et al. [23]

A reverse vortex gliding arc plasmatron is another configuration developed by the research group at Drexel University [24] and further studied by the Plasmant research group in Antwerp [6,25-27]. This configuration uses the concept of a reverse vortex flow, to create a three-dimensional reactive volume and enhanced convection and is shown in Figure 7. The benefits of this configuration are that the plasma deviates further from equilibrium with a higher quench rate. Nunnally et al. attribute the high level of CO_2 conversion efficiency of approximately 43% to increased vibrational excitation of the species in the plasma [24]. A three-dimensional reactive volume also increases residence times, and the reverse vortex enhances stabilization. The downside to this device is its complicated geometry, and no optical access to perform spectroscopic analysis.

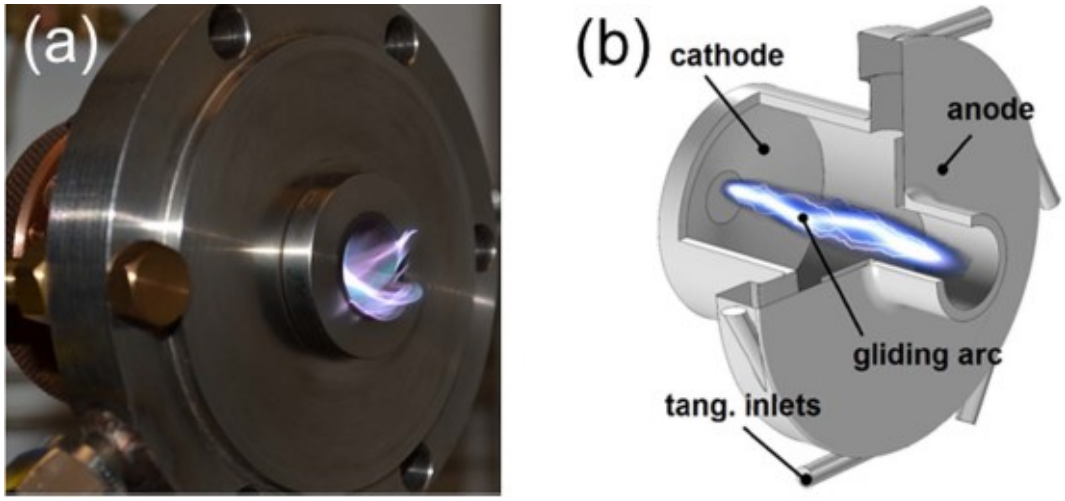

Figure 7. Photograph of the reverse vortex gliding arc plasmatron (left) and schematic drawing of the internal structure (right) developed by the Plasmant research group and taken from Ramakers et al. [6].

Another recently developed configuration of gliding arc consists of two concentric electrodes where the arc rotates and elongates due to a magnetic field seen in Figure 8. Gangoli et al. developed a device that works off the basic principles of gliding arcs called the magnetically stabilized gliding arc discharge (MSGAD) [2]. Using the concept of the critical arc length and knowing that under this characteristic length the gliding arc is completely stable an ideal device

could be developed. It consists of a gliding arc elongated to a magnitude lower than the critical length and then to sustain this arc along infinitely long parallel electrodes. Obviously, this is not realistic, but using a three-dimensional cylindrical configuration this idea could be simulated. Two concentric electrodes are spaced such that at the largest inter-electrode gap, the arc is under the critical length. The gliding arc initiates on a wire that spirals up using the Lorentz force caused by the magnetic field, before becoming anchored at the largest inter-electrode gap. The arc rotates indefinitely because the length of the arc does not surpass the critical length, and the power dissipated from the discharge, ωl stays constant. The power supply never reaches its maximum, thus achieving stabilization along two infinitely long electrodes in a finite space.

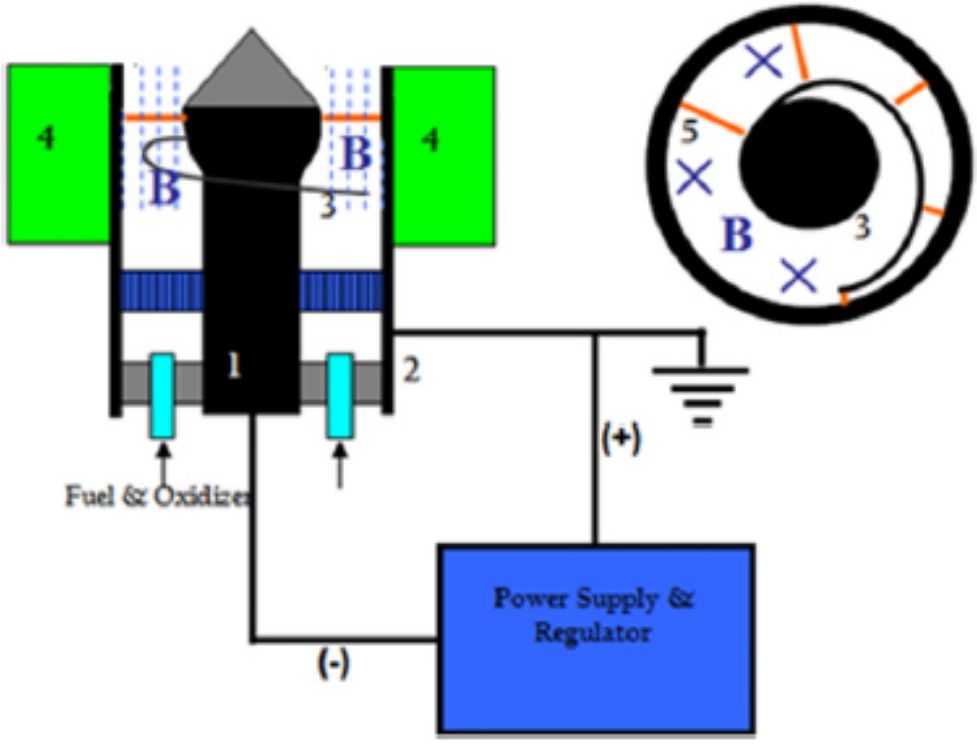

Figure 8. Schematic of the MSGAD setup: 1 - high-voltage cathode, 2 - grounded anode, 3 - wire attached to cathode, 4 - ceramic ring magnets, 5 - top view of discharge. This schematic was taken from Gangoli et al. [2].

Gangoli et al. determined that the MSGAD operates in a region between a traditional glow discharge and an arc discharge [2]. This can be clearly seen on DC voltage-current characteristic plots, where glow discharges typically have a current less than 0.01 A and arc discharges typically

have a current greater than 1 A. Figure 9 displays the voltage-current characteristic of the MSGAD for various flow rates which is compared to glow discharges and arcs. From this plot one can see the expected negative V-I curve of electric arcs, symbolizing a negative differential resistance. Furthermore, the low current ranging between 50 – 150 mA can be seen, which is orders of magnitude smaller than traditional arc discharges.

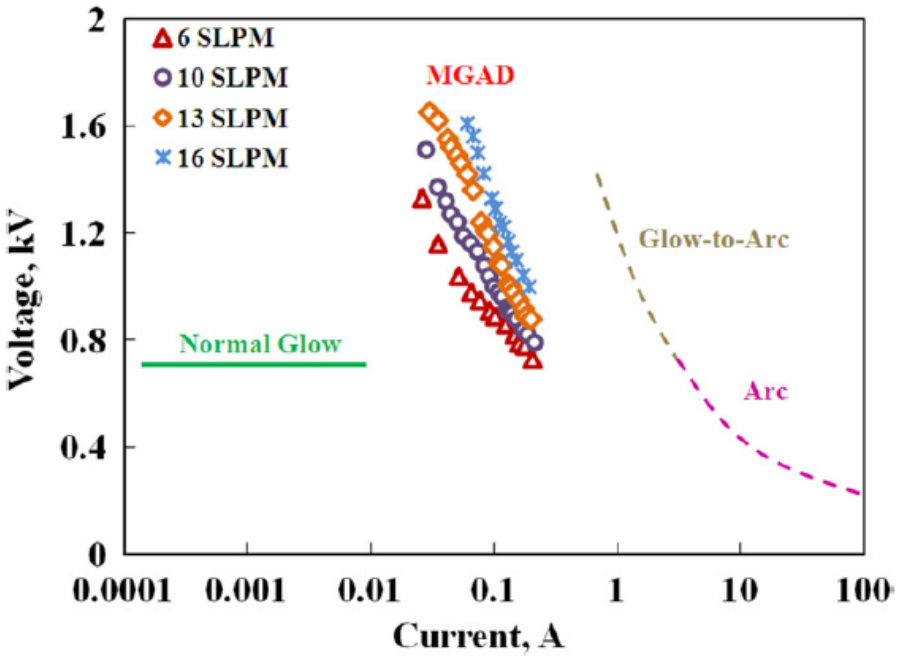

Figure 9. Voltage-current characteristic of the MSGAD at various flow rates. Taken from Gangoli et al. [2].

In a gliding arc plasma column the voltage drop varies linearly along the length, it is only near the cathode and anode where a non-linear voltage drop is witnessed. This allows the electric field to be found for the bulk of the gliding arc, when considering the length of the discharge column and the discharge voltage drop. High electric fields of around $7.5x10^4\ V/m$ were obtained at low operating currents and decreased to under $2.5x10^4\ V/m$ as the operating current was increased [3]. These moderate electric fields further show the different class gliding arcs are in. Arc discharges typically require low electric fields $<\ 1.0x10^4\ V/m$ and glow discharges require high ones $>\ 1.5x10^5\ V/m$ [20]. Gangoli et al. estimated electron temperatures to be 0.8 – 1.2 eV which correlates well with other research groups [3]. From the electron temperatures they found

the number density of the electrons to vary between $1x10^{13} < n_e < 3x10^{14}\ cm^{-3}$ further confirming the non-equilibrium behaviour of gliding arcs.

Further adaptations of this device add a vortex gas flow to aid in the stabilization of the arc [4,5,9,11,12,18]. These consist of a solid conical electrode placed concentrically with a hollow cylindrical electrode. The vortex flow along with magnetic field allows the arc to ignite at the shortest inter-electrode gap and elongate through the diverging electrodes. These are termed rotating gliding arcs (RGA), and have shown to increase residence times, lower electrode degradation and provide a larger more homogenous reactive volume. The current study delves into the arc dynamics of this type of gliding arc and is the only type further discussed. A schematic of the RGA used in this thesis can be seen in Figure 10 and is very similar to devices studied in the literature.

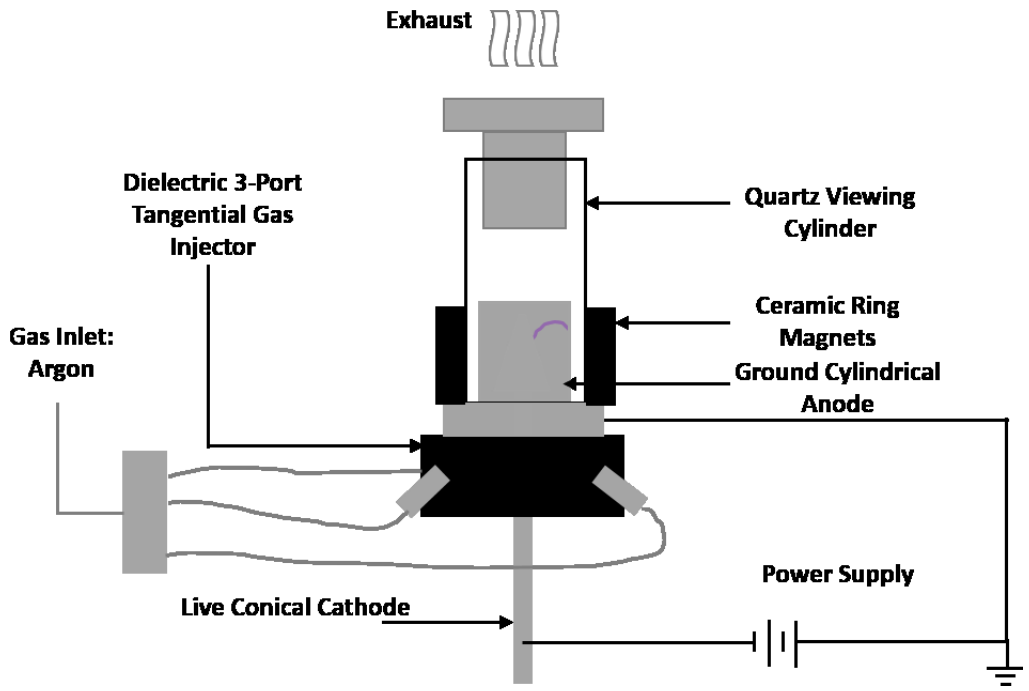

Figure 10. Schematic of a RGA setup used in this thesis.

The main difference between different devices found in the literature is whether or not they use an external magnetic field, what type of power supply they used, or how the gas is injected into the system. One of the biggest design issues rotating gliding arcs face is electrically insulating

the cathode from the anode. To avoid modifying standard cylindrical anodes, the insulation must be provided through the gas injector. Wu et al. studied combustion using a RGA and used a vortex gas ring as the injector. Vortex gas rings are used mainly in various combustion devices, and are able to provide a good flow profile for combustion [9]. The group did not discuss the material the injector was made from, but by looking at the schematic shown in Figure 11 it must be made of some electrically insulating material, such as ceramic.

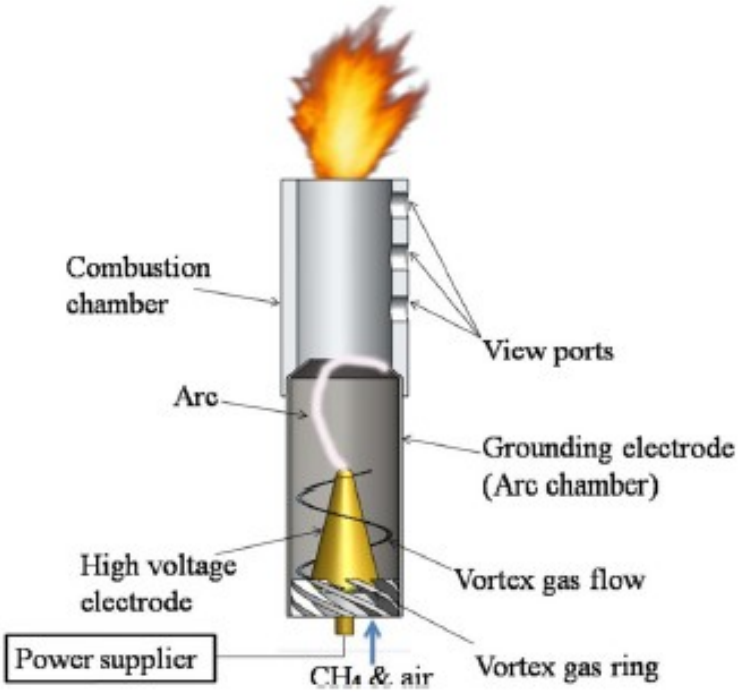

Figure 11. Schematic of rotating gliding arc and vortex gas ring injector used to enhance combustion. Taken from Wu et. al. [9].

Another research group that studied RGA technology modified the cylindrical anode to contain tangential inlets near the base of the conical electrode [4,5,12,18]. To insulate the two electrodes a Teflon™ (PTFE) base is connected to the anode. To provide a magnetic field, field coils and a supplementary power supply were used. The schematic of the device can be seen in Figure 12.

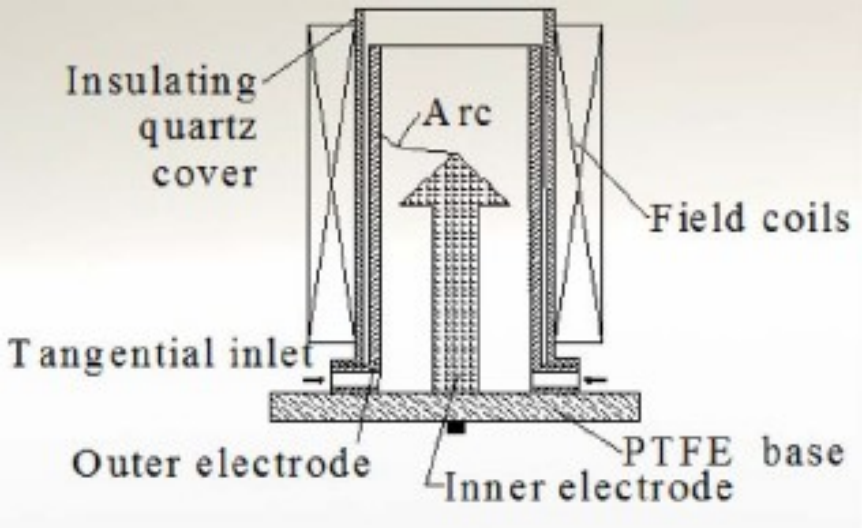

Figure 12. Schematic of rotating gliding arc with tangential inlets directly on cylindrical anode. Taken from Zhang et al. [4].

The device used a DC power supply and depending on the gas used changed the voltage and current characteristic. The first paper studies air and nitrogen as the operating gas. With a shortest inter-electrode gap of 3 mm, the air and nitrogen breakdown at a similar voltage of approximately 2500 V. This discharge was sustained with low currents of approximately 160 – 200 mA. The restrike frequency and stability was largely affected by the carrier gas. Figure 13 shows the effect changing the gas composition had on the voltage and current of the discharge. Nitrogen is shown on the left and has a much more irregular breakdown pattern when compared to air, but both follow the same trend. Breakdown occurs at high voltages of ~ 2500 V. This is accompanied by a drastic voltage drop to ~ 1000 V and a current rise. The arc is now initiated at the shortest inter-electrode gap and begins to elongate. During elongation the voltage will rise as the current falls, giving rise to a negative voltage-current characteristic, typical for an arc. The power supply will eventually reach a point where it can no longer sustain the length of the arc, and breakdown will occur again, re-initiating an arc at the shortest inter-electrode gap. When air is used as the gas, the discharge cycle occurs with more or less the same frequency, which the authors attribute to more radicals being in the discharge [4].

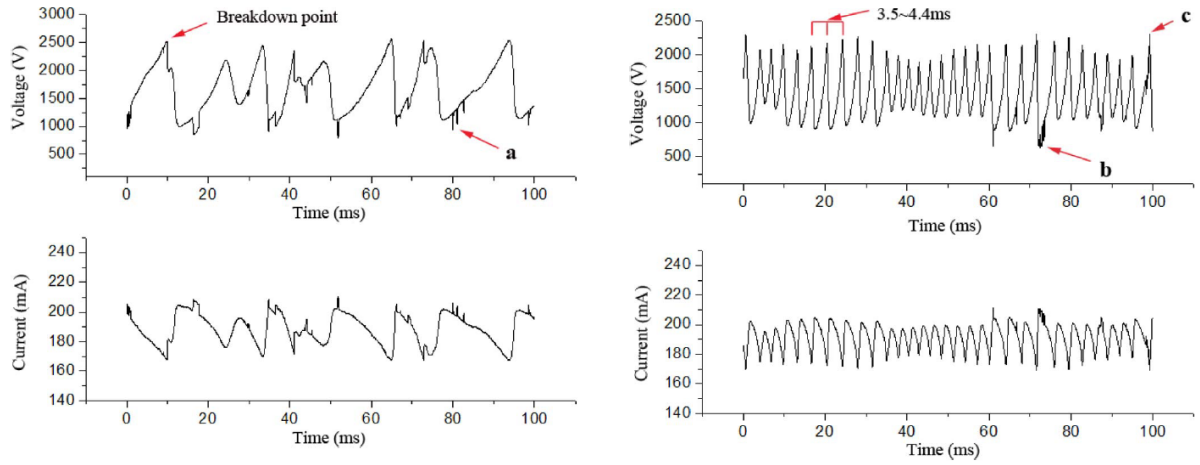

Figure 13. Voltage and current waveforms at a gas flow rate of 8.3 SLPM with nitrogen (left) and air (right) as the carrier gas. Taken from Zhang et al. [4].

This device was further tested with other gas compositions that changed the voltage and current waveforms. When methane-nitrogen mixtures are used the restrike frequency increased drastically, and became quite stable. The mixture contained 20 mol % methane.

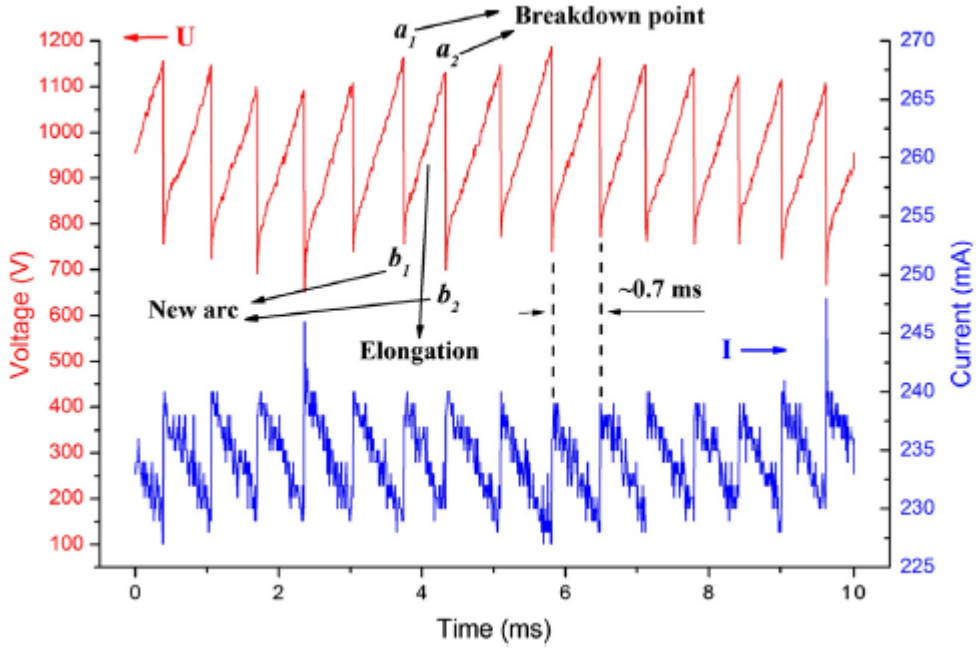

Figure 14. Voltage and current waveforms of a methane-nitrogen mixture at a flow rate of 12 SLPM. Taken from Zhang et al. [28].

The benefits of this system are associated with the use of a single high-voltage, high-current DC power supply to sustain the discharge. It consisted of a 10 kV output, in which a large ballast resistor of 40 kΩ is used to limit the current into the device. This allowed the arcs to be continuously active with no down time, however power supplies of this calibre are quite expensive [4].

2.2.3. Forces Acting on the Rotating Gliding Arc

In a rotating gliding arc with accompanying magnetic field there are two ways arc motion can be induced, a gas flow into the device or motion induced via a magnetic field. The following derivation was proposed by Gangoli et al. [2] and further developed by Zhu et al. [18]. Therefore, the two main forces acting on the arc column at any given time are the aerodynamic drag force, and the Lorentz force. The difference in viscosity of the plasma column compared to the bulk gas, generates a drag force acting on the more viscous column. The drag force acts in the same direction of the fluid flow. The arc column is also a current carrying cylinder, thus the application of an external magnetic field results in a Lorentz force acting on the column. Both forces can be used to describe the motion of the arc through the device.

The aerodynamic drag $\vec{F}_{D,\theta}$, in the azimuthal θ direction can be found per unit length of the arc column with the drag coefficient C_d, the gas density ρ, the relative azimuthal arc velocity $\vec{u}_\theta = (\vec{u}_{arc,\theta} - \vec{u}_{gas,\theta})$, and the arc column diameter D_a.

$$\vec{F}_{D,\theta} = \frac{1}{2} C_d \rho \vec{u}_\theta^2 D_a \tag{21}$$

The Lorentz force $\vec{F}_L$, can be found per unit length of the arc column with the discharge current $\vec{I}_D$, and the magnetic field strength $\vec{B}$, as follows.

$$\vec{F}_L = \vec{I}_D x \vec{B} \tag{22}$$

The external magnetic field is oriented along the main axis of the coaxial cathode-anode arrangement and the current is flowing through the arc column. Therefore, the resulting force acting on the arc column aids in the rotation of the arc. The following figure depicts the forces acting on the arc column in a rotating gliding arc.

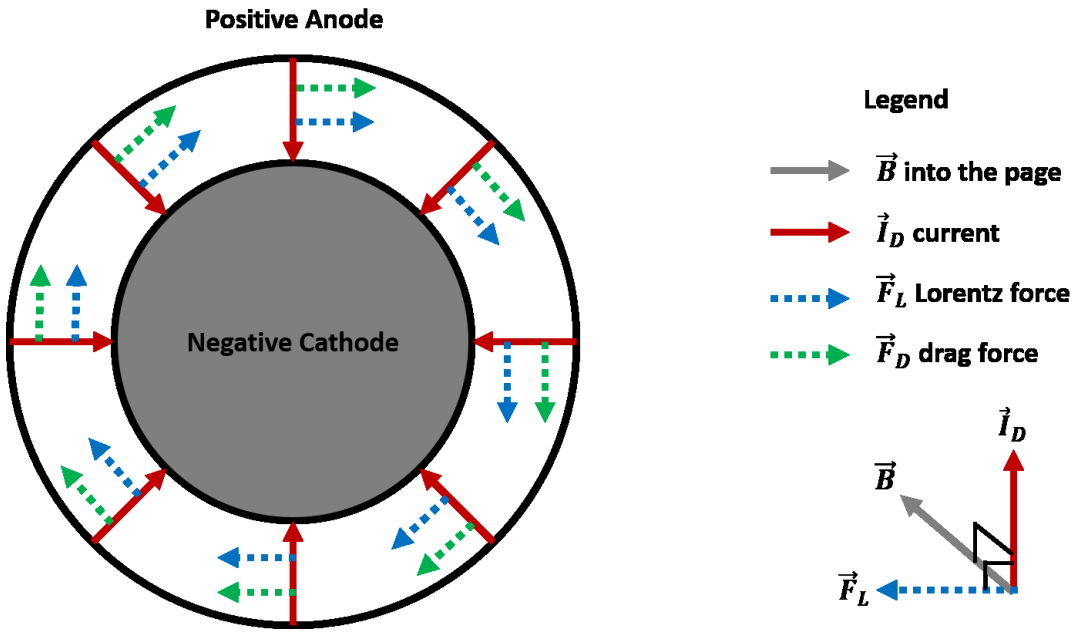

Figure 15. Face-down schematic of the coaxial cathode-anode assembly used in this thesis and the forces acting on the gliding arc column.

Assuming steady state, where the arc is not accelerating, but rather in motion with a constant velocity, the Lorentz force and the aerodynamic drag balance one another, $\vec{F}_{D,\theta} = \vec{F}_L$. From this, a relationship between the frequency of arc rotation, discharge current and gas velocity can be found, where D is the inside diameter of the cylindrical anode.

$$f = \frac{\vec{u}_{arc,\theta}}{\pi D} = \frac{1}{\pi D}\left(\sqrt{\frac{2I_D B}{C_d \rho D_a}} + \vec{u}_{gas,\theta}\right) \tag{23}$$

A study of the forces acting on rotating gliding arcs was conducted by Gangoli et al. with their magnetically stabilized gliding arc discharge [2,3]. Using a high-speed camera they measured the rotation frequency of the gliding arc that was operated in air. The inside diameter of the anode was 30 mm, they used a magnetic field strength of 0.12 T, estimated the air density to be 1.29 kg/m^3 and used a drag coefficient of 1.3. The model they used was slightly different than the one proposed in this thesis. For the aerodynamic drag force they did not include the $1/2$ factor as seen in equation 21. Figure 16 displays the experimental and simulated frequency of arc rotation for the device. The obtained frequencies were quite low because the gas flow rate was not aiding in the

rotation of the arcs in this device configuration. The gas was supplied to the device axially, and the arcs rotation was solely induced via the magnetic field. Therefore, for modelling purposes the magnitude of $\vec{u}_{gas,\theta}$ in equation 23 can be assumed to be zero.

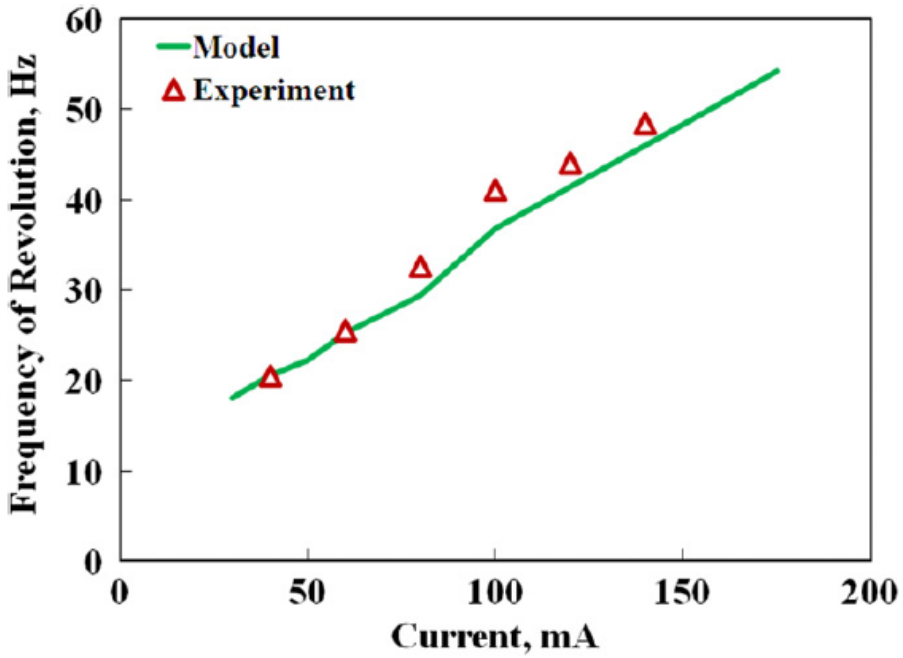

Figure 16. Frequency of arc rotation versus current for the MSGAD taken from Gangoli et al. [2].

Gangoli et al. also briefly described the arc column diameter and the length of the arc column at low flow rates. They found that at low flow rates of 4 SLPM the arc column diameter varied slightly between 0.4 – 0.8 mm. They also measured the size of the negative glow located on the cathode of the device, and found that this value increased with an increase in discharge current. The length of the arc column was also found for these operating conditions to be increasing with an increase in arc current. Figure 17 shows the plasma diameter and plasma length plotted against the applied current for this experiment.

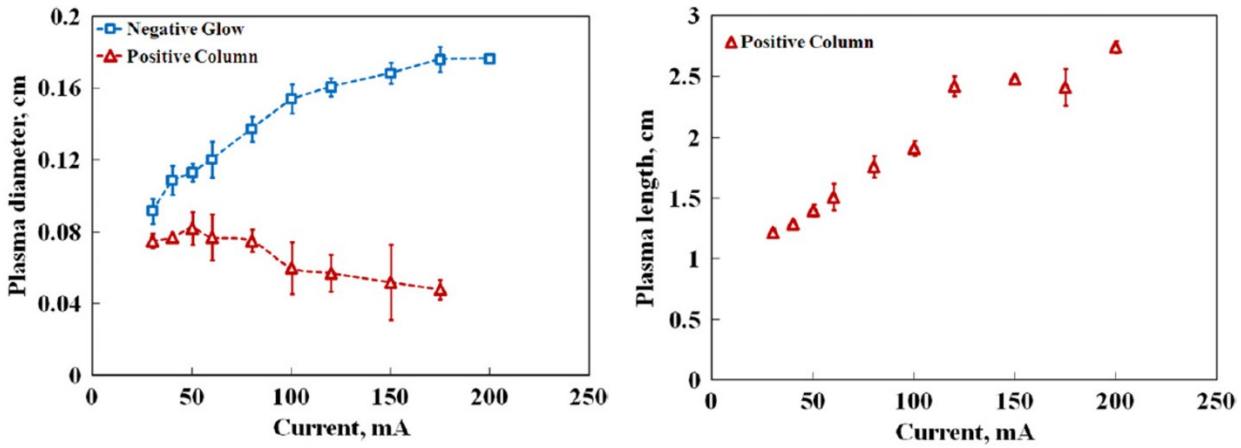

Figure 17. Physical arc characteristics in the MSGAD. Plasma diameter (left) and plasma length (right) versus applied current at a flow rate of 4 SLPM. Taken from Gangoli et al. [3].

Recently Zhu et al. further characterized the physical arc dynamics of a rotating gliding arc (RGA) with magnetic field and vortex flow field. [18] The discharge was ignited in nitrogen and the arc motion was characterized using a high-speed camera. The magnetic field strength was lower in this experiment, being only 0.1 T and they estimated the drag coefficient to be 1.1. The diameter of the cylindrical anode was 36 mm and the arc column diameter was measured to be approximately 2 mm which is quite large when comparing diameters obtained by Gangoli et al. The density was assumed to be 1.14 kg/m^3 and this device has a gas flow that aids in the rotation so $\vec{u}_{gas,\theta}$ in equation 23 cannot be assumed to be zero. Using a fluid simulation software they determined the magnitude of $\vec{u}_{gas,\theta}$ to be 0.16 m/s in the θ direction. For this experiment they calculated the rotation frequency to be 14.4 Hz which was close to their experimental result of 18.5 Hz. The following figure displays the time evolution of one arc rotation separated by 6 ms in time.

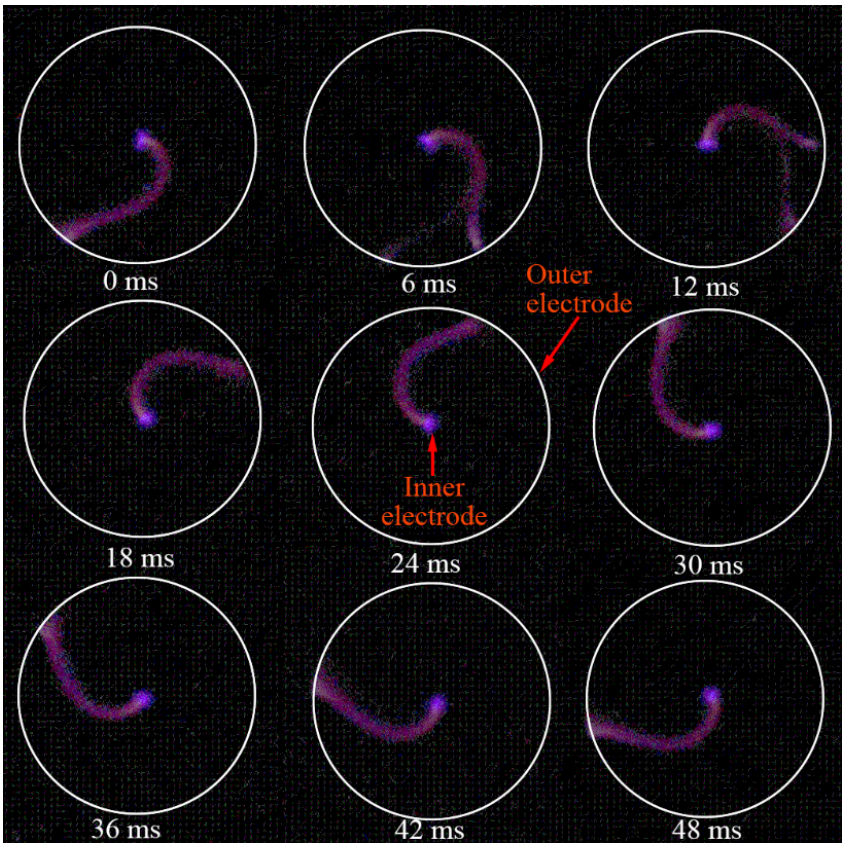

Figure 18. Time evolution of arc motion using a high-speed camera at 5000 frames per second. Discharge ignited in nitrogen, taken from Zhu et al. [18].

Both of these studies provide a brief overview of the arc dynamics of a rotating gliding arc stabilized by a magnetic field. The main similarity is the operation in a nitrogen rich plasma, with an arc that rotates at a fixed location at the tip of the cathode. The diameter of the anode for both cases is almost double the diameter used in this thesis.

Chapter 3. Experimental

3.1. Rotating Gliding Arc Device

A photograph and schematic of the rotating gliding arc device are shown in Figure 19. A conical cathode is mounted concentrically inside a grounded hollow cylindrical anode. Both electrodes are made of stainless steel 304 and the shortest inter-electrode gap is 1.66 mm. The two electrodes diverge downstream to the largest inter-electrode gap of 7.20 mm. The overall length of the cone is 25.4 mm. The hollow cylindrical anode as well as the downstream exhaust assembly consist of standard CF 1-1/3 fittings (MDC Vacuum^{TM}, USA), with an inner diameter of 16.23 mm. Three 1/16" (1.59 mm) tangential inlets feed the plasma forming gas at an angle of 29º axially, and 30º radially to the system thus providing a clockwise vortex flow up and around the conical cathode (as viewed from the top of the assembly). While the gliding arc is active, the temperature of the gas, and consequently its viscosity, is higher within the column than in the surrounding gas. The cold gas vortex flow acts on the more viscous gas region and drags it along, thus aiding the rotational movement. A rotameter is used to adjust the argon gas flow rate up to a maximum of 30 SLPM. Electrical insulation between the electrodes is provided by a thermoplastic spacer (Polyoxymethylene, Delrin^{TM}) which also holds the gas injectors. Four low-cost ceramic (ferrite) ring magnets (7.1 mm-thick each, McMaster-Carr, USA) placed outside of the anode provide a static axial magnetic field. The application of the static magnetic field along the axis of the device while the arc is present in the inter-electrode gap results in a Lorentz force acting in the azimuthal direction, thus acting along with the vortex flow to drive the gliding arc into a rotational movement around the conical cathode. The magnets can be flipped around such that the Lorentz force acts against the aerodynamic drag caused by the gas vortex. The stack of ring magnets gives rise to a magnetic field strength of ~1220 G (0.122 T) on the axis and ~430 G (0.043 T) on the inner surface of the stack. The RGA device is exhausted through a confined assembly to avoid external gas entrainment. Optical access is provided by a quartz sleeve located immediately downstream (side view), and a quartz viewport facing the RGA inter-electrode gap.

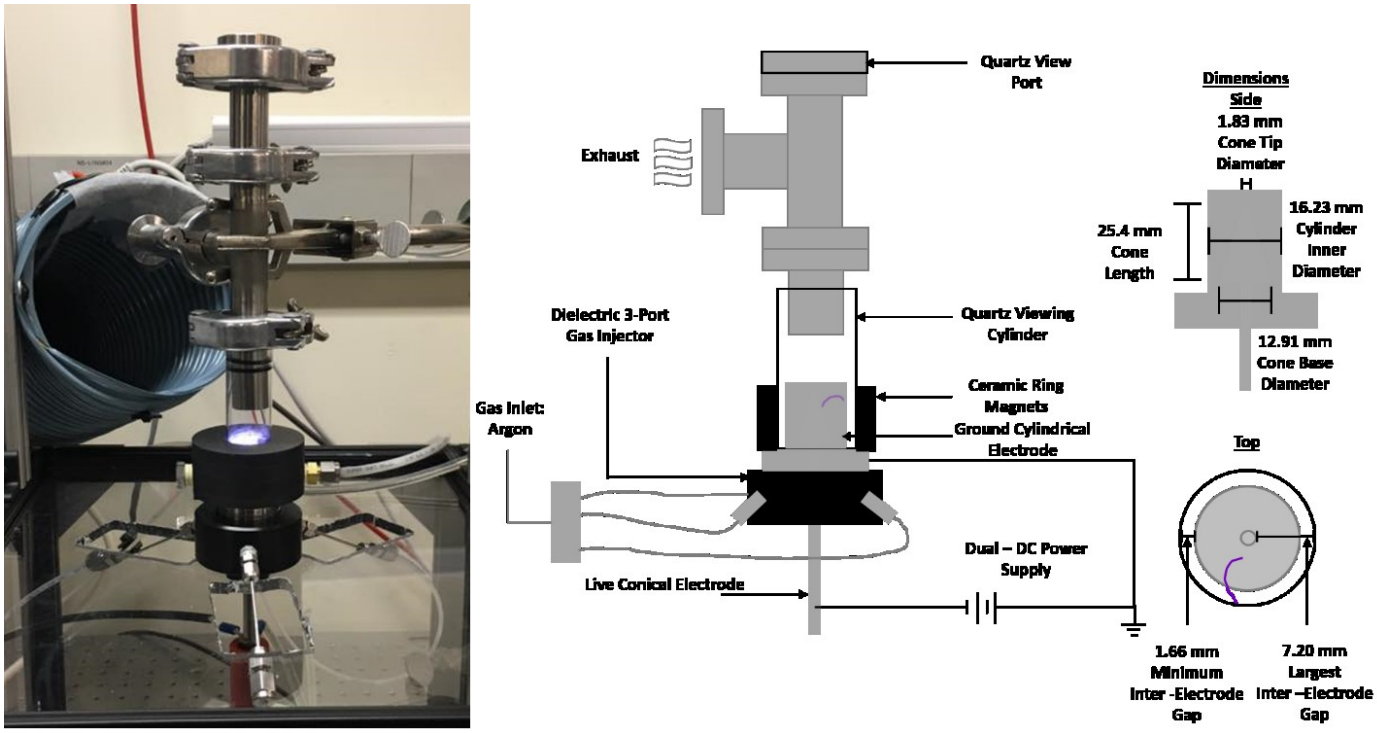

Figure 19. Rotating gliding arc set-up. Left: RGA in atmospheric pressure argon. Right: Schematic with characteristic dimensions.

3.2. Rotating Gliding Arc Power Supply

To initiate breakdown a voltage greater than the breakdown voltage is required to produce a spark. Once a conductive channel is produced, current can be fed across the electrodes to allow the arcs to elongate. The rotating gliding arc is operated with argon at atmospheric pressure and in this study the shortest inter-electrode gap, where the spark channel initiates is 1.66 mm. Based on this and knowing that the minimum electric field is on the order of 10-20 kV/cm the expected breakdown voltage should be approximately 2000 V.

The power supply which can provide the current needed to sustain the arcs is only capable of reaching 1000 V, therefore a separate high voltage power supply is required. To initiate breakdown in this study a Cockcroft-Walton voltage multiplier (CWVM) is used to convert a low-voltage AC source into a high-voltage DC signal. Once the CWVM discharges, a capacitor charging power supply connected in parallel begins to operate and feeds current to the discharge.

3.2.1. Cockcroft-Walton Voltage Multiplier

Cockcroft-Walton voltage multipliers are useful circuit elements for many different reasons. Popularized in 1932 by Cockcroft and Walton [30] the circuit element rectifies and amplifies a low-voltage with simple and inexpensive passive circuit elements. These multipliers can reach several thousand kV [30] with the right set-up, providing overall low voltage stress on the capacitors and diodes used, with high efficiencies. The only drawbacks include large voltage ripples at the output and voltage drops. [31] For the application of a rotating gliding arc however, voltage drops, and voltage ripples are not an issue. As long as the breakdown voltage is reached, the CWVM can be used. The following analysis of the CWVM was taken from [31] unless otherwise stated.

Figure 20 shows a basic 2-stage negative polarity Cockcroft-Walton voltage multiplier circuit. An input source voltage, V_{CW} is applied and each half cycle of the sinusoidal wave charges certain capacitors, with diodes restricting or allowing the flow of charges during the negative and positive half cycles. $D1$ being forward biased, allows only positive current to flow through, charging $C1$ to a value of V_{CW}. When the polarity changes, current may flow through the reverse biased $D2$, charging $C2$ up to a total of $-2V_{CW}$ ($-V_{CW} - C1$). Each change in polarity causes a cascading effect where every capacitor is charged to $-2V_{CW}$, except for $C1$ which stays at V_{CW}. Due to the capacitors between the load and ground being in series ($C2$ & $C4$), the output voltage is the sum of the charged capacitors voltage, giving an overall voltage drop that is a function of the stages added in series. The theoretical maximum voltage can be represented by the following simple formula, where n is the number of stages, in which each stage consists of two diodes and two capacitors, V_{CW} is the peak applied AC voltage and V_{Load} is the output DC voltage.

$$V_{Load} = 2nV_{CW} \tag{24}$$

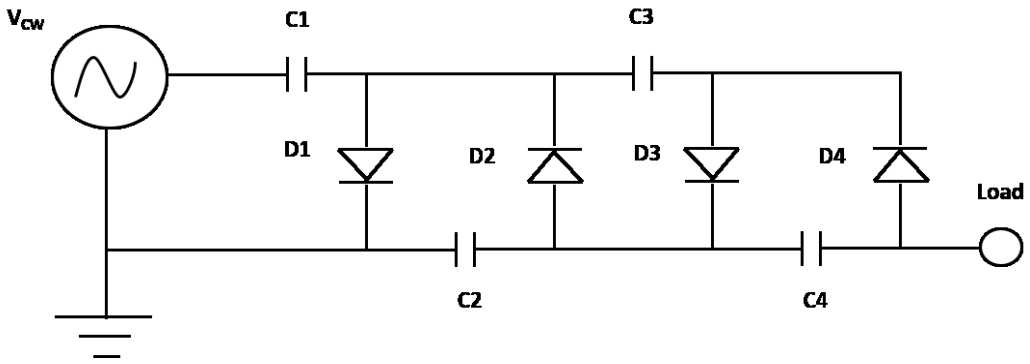

Figure 20. Schematic of a 2-Stage negative polarity Cockcroft-Walton voltage multiplier.

Increasing the number of stages shows diminishing returns due to a sagging effect lowering the actual output voltage and creating a voltage ripple. This occurs when the load draws some amount of current from the circuit element, specifically the capacitors between the load and ground. Even though the output is DC each cycle of the AC input causes the output to reach a maximum and minimum ripple. The magnitude of this ripple can be defined as $2\delta V$ and each capacitor ($C2$ & $C4$) provides some portion of this. Looking at a single capacitor, namely C_{2n}(all even numbered capacitors) and the charge transferred from the capacitor to the load per cycle q, the voltage ripple can be found.

$$2\delta V_{2n} = \frac{q}{C_{2n}} \tag{25}$$

At the same time charges are transferred from C_{2n-2} to the load and to C_{2n-1} providing the following voltage ripple:

$$2\delta V_{2n-2} = \frac{2q}{C_{2n-2}} \tag{26}$$

A cascade charge addition pattern is forming, where the sum of all the voltage ripples from each capacitor can be shown as follows:

$$2\delta V = q\left(\frac{1}{C_{2n}} + \frac{1}{C_{2n-2}} + \cdots + \frac{1}{C_2}\right) \tag{27}$$

Most Cockcroft-Walton voltage multipliers operate with the same value capacitance at every stage and the one used in this study does as well. Knowing that the charge transferred is

equal to the ratio of the load current I and the AC frequency f, a simplified voltage ripple can be defined.

$$2\delta V = \frac{I}{fC}\left(\frac{n(n+1)}{2}\right) \tag{28}$$

During each cycle of the sinusoidal wave when a load is connected to the circuit a small portion of voltage is lost to this voltage ripple effect. Therefore, the previous maximum defined in equation 24 contains a voltage drop equivalent to the amount of charge lost to the ripple. The voltage drop at each capacitor in series between the load and ground can be shown as follows.

$$\Delta V_2 = \frac{q}{C}n,$$

$$\Delta V_4 = \frac{q}{C}[2n + (n-1)], \cdots \tag{29}$$

$$\Delta V_{2n} = \frac{q}{C}[2n + 2(n-1) + \cdots + 2x2 + 1]$$

Then by adding up every voltage drop a total voltage drop can be determined.

$$\Delta V_{Load} = \frac{I}{fC}\left(\frac{2}{3}n^3 + \frac{1}{2}n^2 - \frac{n}{6}\right) \tag{30}$$

Therefore, when a load is connected to the CWVM the maximum output voltage is:

$$V_{Load} = 2nV_{CW} - \frac{I}{fC}\left(\frac{2}{3}n^3 + \frac{1}{2}n^2 - \frac{n}{6}\right) \tag{31}$$

When applying this concept to producing sparks in a rotating gliding arc a few conclusions can be made. The load current is dependent on the spark channel that is created between the two electrodes. Since it likely ignites at a similar location inside the device, this load current is fixed. When designing the circuit for spark ignition the only parameters that can be varied are the applied AC voltage, frequency, capacitance of each capacitor and number of stages. Obviously, the higher the AC voltage the higher the output, with no effect on voltage drop, so ideally this should be maximized. The higher the frequency and the higher the capacitance the lower the overall voltage drop is, so maximizing this is ideal. The number of stages affects both the maximum output as well as the voltage drop. Therefore, to be more efficient this should be minimized, while still reaching a high enough output (ie. 2000 V). An efficient circuit would be to use a high voltage

supply with less CW stages as outlined by Malik et al. who used a Cockcroft-Walton multiplier for nanosecond plasma processing [32]

3.2.2. Series RC Circuit

The basic operating principle of the rest of the power supply is quite simple as it encompasses two different series RC circuits. A series RC circuit consists of a power supply connected to a resistor and a capacitor. These circuit elements are used to control the amount and rate of current that can flow to the device. This section was cited from *The Art of Electronics* unless otherwise stated [33].

Capacitors are passive devices that store energy in the form of an electric field. They act similarly to a battery in that they can build up, store and release electrical energy. When a capacitor has no charge, it maintains a voltage of zero, however when it is charged up by means of a supplementary power supply it maintains a voltage equivalent to the power supply across its terminals. Figure 21 displays a simple series RC circuit diagram. When a discharged capacitor is initially at zero volts and the circuit is closed current starts to flow rapidly across the capacitor starting to build up the voltage rapidly. Over time, the capacitor eventually reaches the same potential as what was applied. However, as the capacitor voltage approaches this it does so at a slower rate, due to the current being lower. This means that in a RC circuit the charging voltage curve follows a logarithmic trend over time and the current follows the inverse.

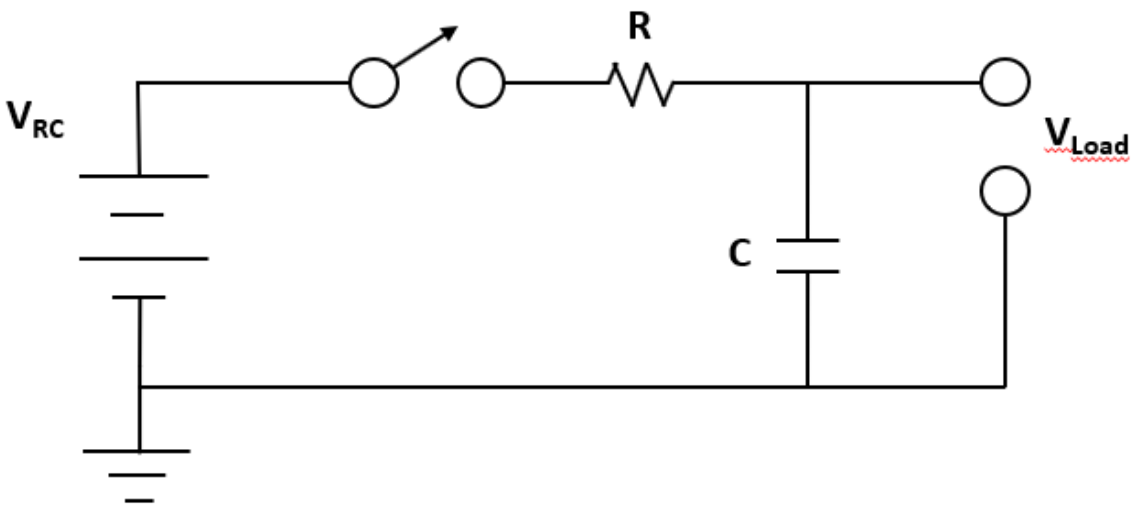

Figure 21. Schematic of a simple series RC circuit

The equation that governs the above circuit is as follows, where I is the current, C is the capacitance, R is the resistance, V_{RC} is the power supply voltage, and V_{Load} is the output voltage across the capacitor.

$$I = C\frac{dV_{Load}}{dt} = \frac{V_{RC} - V_{Load}}{R} \tag{32}$$

Rearranging and integrating gives the solution in the form.

$$V_{Load} = V_{RC}\left(1 - e^{-t/RC}\right) \tag{33}$$

The time constant of the circuit, $\tau = RC$, governs the time it takes for the capacitor to charge and discharge. Eventually, when the time is much greater than the time constant (~ 5τ) the capacitor is fully charged and V_{Load} is equal to V_{RC}.

When the capacitor discharges, it follows the inverse trend as when it charges. This means that the voltage rapidly falls at the start and slow down as time goes on. The following equation defines a discharging capacitor in an RC circuit.

$$V_{Load} = V_{RC}\, e^{-t/RC} \tag{34}$$

3.2.3. Circuit Used in this Study

The power supply consists of a homemade two-stage unit: A high-voltage arc igniter (Figure 22, top) combined with a current driver (Figure 22, bottom). The arc igniter consists of a Cockcroft-Walton (CW) voltage multiplier which converts a low-voltage high frequency AC signal (peak voltage V_{CW}) to a pulsed high voltage negative DC signal. We used a variable frequency-low output voltage AC source (ENI Power Systems Model EGR 800). Due to this low maximum voltage, a 35 stage Cockcroft-Walton multiplier was needed to reach an output voltage of ~10 kV_{peak}. This unit was built with 0.1 μF capacitors and 1 kV/1A diodes. A more efficient alternative would be to use a higher voltage supply with less CW stages as outlined by Malik et al. [30]. The RC discharge time constant of the Cockcroft-Walton voltage multiplier is τ_{CW} ~2.5 ms. At this point the current driver takes over and feeds the required gliding arc current to the system while providing enough voltage for the arcs to elongate and glide through the inter-electrode gap. This unit consists of a simple RC circuit driven by a 2.5 kW negative polarity capacitor-charging power supply with a -1000 V open circuit voltage (Analog Modules, Inc. model 5743). A high-energy capacity capacitor of 10 μF is charged through a 75 Ω resistor, and partially discharged to the gliding arcs through a 2 kΩ resistor (discharge time constant of τ_C ~20 ms, without considering the resistance from the gliding arc). Two additional high-voltage diode sets are used to prevent high voltage or current exposure on each power supply.

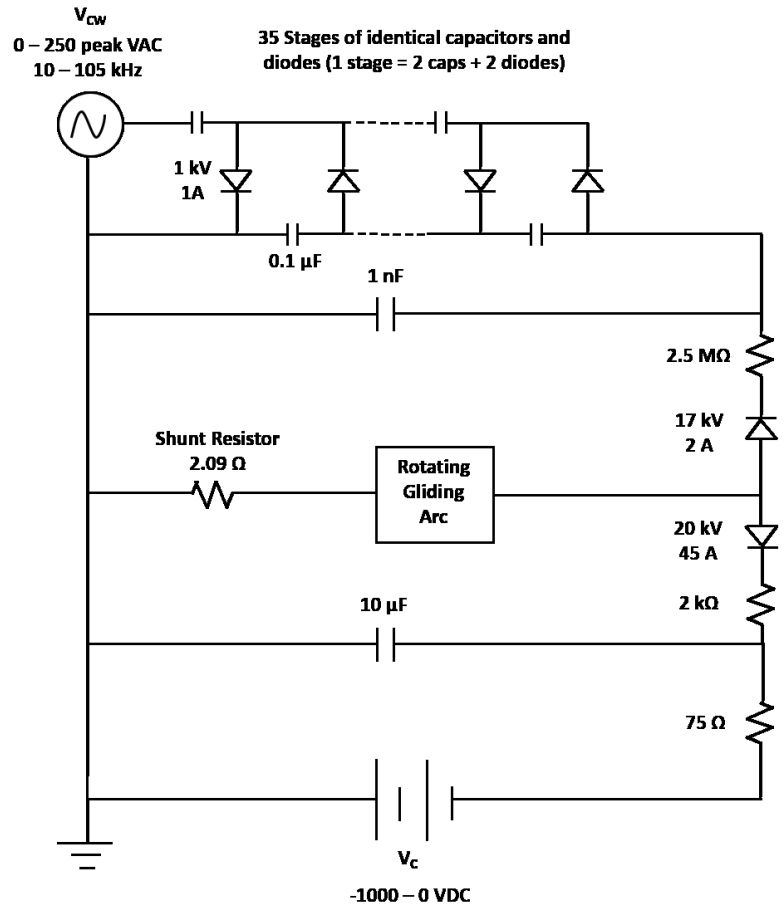

Figure 22. Homemade power supply used to drive the arcs. Cockcroft-Walton generator (top), current-driver RC circuit (bottom).

3.3. Experimental Set-up

To characterize the RGA dynamics, a combination of electrical measurements and high-speed imaging is carried out. Figure 23 shows a schematic of the instrumentation used. The RGA voltage, V_D (V), is measured using a passive high voltage probe (Tektronix P6015A) while the discharge current, I_D (A), is measured using a passive voltage probe (Tektronix P2200) across a 2.09 Ω shunt resistor. Both signals are acquired and displayed with a digital oscilloscope (Tektronix TDS 2024) with a sampling rate of 2GS/s. A high-speed camera (Fastcam Photron SA5) looking at the inter-electrode gap face-on is used to image the rotating arcs. The camera is set to 20000 frames per second, with a shutter speed of 1/20000 s, thus providing clear images at

a resolution of 256 x 256 pixels. The oscilloscope and camera are both synced to record the instantaneous arc voltage and circuit current, and corresponding gliding arc image.

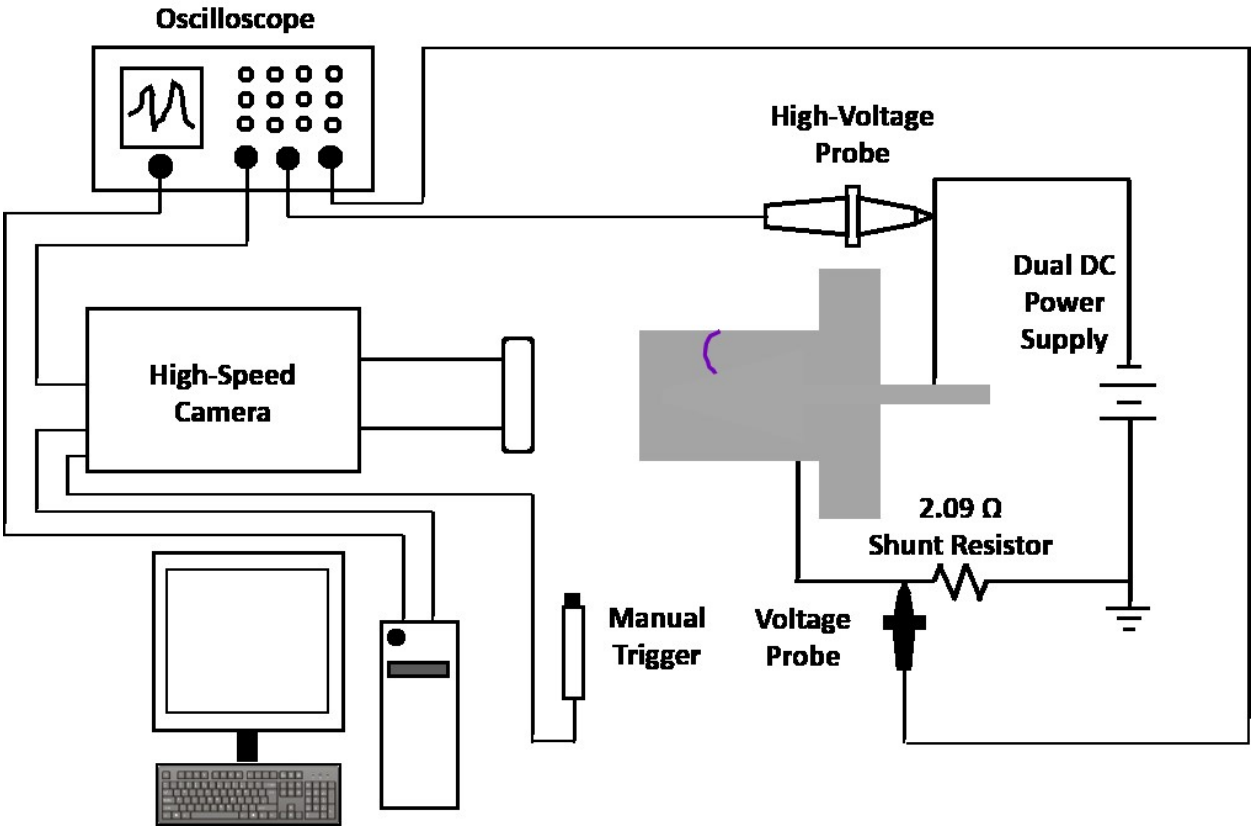

Figure 23. Schematic of the instrumentation.

For this study, the AC voltage signal supplied to the Cockcroft-Walton generator was set at V_{CW} = 80 V_{peak} and 35 kHz. The input voltage of the capacitor charging power supply (V_C) and the total flow rate of 99.998% purity argon (Q, $Q/3$ in each injector) were varied from -300 to -500 V, and from 0.0 to 26.3 SLPM, respectively.

3.4. Image Analysis Technique

In this study a high-speed camera is used to capture the arc motion behaviours and compare to the electrical signals. The output of the high-speed camera is a video that consists of a defined

number of frames. For most experiments conducted a frame rate of 20000 frames per second is used with a shutter speed of 1/20000 s. These were found iteratively to produce the clearest evolution of the arc at all operating conditions. Based on the mount used for the camera, the most suitable resolution to capture the events is 256 x 256 pixels. The camera has a built-in trigger system, to sync up the recordings with the electrical measurements. The breakdown of one recording is quite simple. The camera is attached to the oscilloscope such that when the image is taken it would send a signal to the oscilloscope displaying the initial and final frame. This occurs whenever the manual trigger or the button on the program on the computer is applied. The initial and final frame provide enough information to find the discharge voltage, current and arc motion with respects to time.

To analyse the video files, a series of image analysis techniques are required. All of the image analysis is conducted using MatLab^{TM} and begins by breaking the video down into each individual frame. The algorithm used for all the videos is first initialized on a single frame. Figure 24 displays a single frame obtained from one of the trials, that was modified slightly to include the outline of the electrodes. The camera is set such that the aperture is almost fully closed. The reason for this is to only receive bright light from the arc column, giving a well-defined column. The drawback to this is that there is not enough light on the electrodes for them to be detected. Therefore, once the settings are correct an initialization snapshot is taken with the light on, so the electrodes can be seen. The outline of the electrodes are then drawn onto the video as seen in the figure. The dotted red lines indicate the live conical cathode base and tip and the solid white lines are the inner and outer diameter of the cylindrical anode.

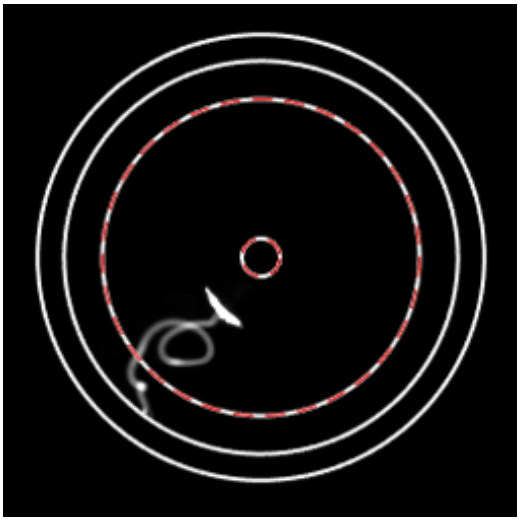

Figure 24. Single frame obtained from the high-speed camera.

Each frame is a 256 x 256 grid with some intensity of light found at individual pixels. If the arc is extinct the frame would be seen with very little detected light. Therefore, these frames were simple to characterize. If the sum of all of the pixels was under a low number (~50000 in this case), the algorithm indicates that frame as being extinct. However, if there is an active arc, determining properties requires some more thought. The cathode root and the anode roots are the most important locations on each frame. The anode is quite simple to find, as it is confined to the inner diameter of the cylindrical electrode. Therefore, location-based thresholding is used to pinpoint the node. The cathode root is much more difficult. It can be situated anywhere on top of the conical cathode, or the edge of the base at the shortest inter-electrode gap. This is a large area to scan, and in most cases the arc column is also located in this area. Fortunately, the cathode spot was always the brightest spot of any frame. The reason for this could be due to ionic bombardment of the cathode, causing sputtering and increased photon emission, or thermionic or field emission. Therefore, to pinpoint this location a location threshold is applied first to remove some of the unnecessary pixels and reduce computing time. Then an intensity-based threshold is applied to find the highest intensity pixels. This gives the large cathode spot as an output, however sometimes the bright nodes in the arc column are detected. The last threshold applied is then to find the largest agglomeration of bright pixels, closest to the tip (center) of the cathode. After all of these simplifications the cathode spot is found. The algorithm used for this analysis can be found in the appendix.

With each of these spots localized, the projected arc length is calculated using Dijkstra's algorithm (a shortest path algorithm), modified to give precedence to pixels with high intensity values (the arc column) [34]. This gives an output of pixel length which is simply converted to a length in mm. The height of the cathode spot can then be found to see the effect different operating conditions has on driving the arc through the device. This is found using basic trigonometry and the knowledge that the cone has an angle of 16.5º from the base to the tip. From this, the vertical height in which the cathode spot is in the device can be found. The last calculation that can be performed is the frequency of arc rotation. For this, four locations on the frame are initiated as counting lines. The algorithm set-up counts the amount of times the anode spot encounters one of these locations and notes the time. If the frequency of rotation is too low, the anode spot can hit the counter lines more than once per actual count. To overcome this, groups of counts that are within a short period of time are considered only once. The frequency of arc rotation is then found using the following equation.

$$f_{Rot} = \frac{Count_{total}}{Time_{end} - Time_{start}} \tag{35}$$

Here, $Count_{total}$ is the number of times the anode spot hit the counter lines, and the time difference is between the time when the last count is found, and when the first count is found. Therefore, using four counting lines on a single video and computing the average, an accurate frequency of rotation can be found.

Chapter 4. Results and Discussion

4.1. Electrical Analysis

Figure 25 reports typical measured voltage and current signals, $V_D(t)$ and $I_D(t)$, obtained during stable operation of the RGA. The instantaneous discharge power, $P_D(t) = V_D(t)\, I_D(t)$, was calculated and added to the figure. One notices that the power supply provides a relatively stable repetitive operation of gliding arcs. During its lifetime, the gliding arc elongates, as observed with the slight increase in arc voltage, and the circuit current decreases while maintaining a relatively constant power. For this trial at a low current-driver voltage (-300 V) and low flow rate (8.8 SLPM), the RGA duration ranges from ~10 to ~40 ms, while its voltage, current and power are ~-250 V, ~-40 mA and ~10 W. The average power is calculated using Equation 37, where T is the total time frame observed (typically 500 ms):

$$P_{avg} = \frac{1}{T}\int_0^T V_D(t)\, I_D(t)\, dt \tag{36}$$

The RGA restrike frequency was calculated from the $V_D(t)$ signal of each trial. The ratio of the number of restrike events and the time elapsed gave the restrike frequency.

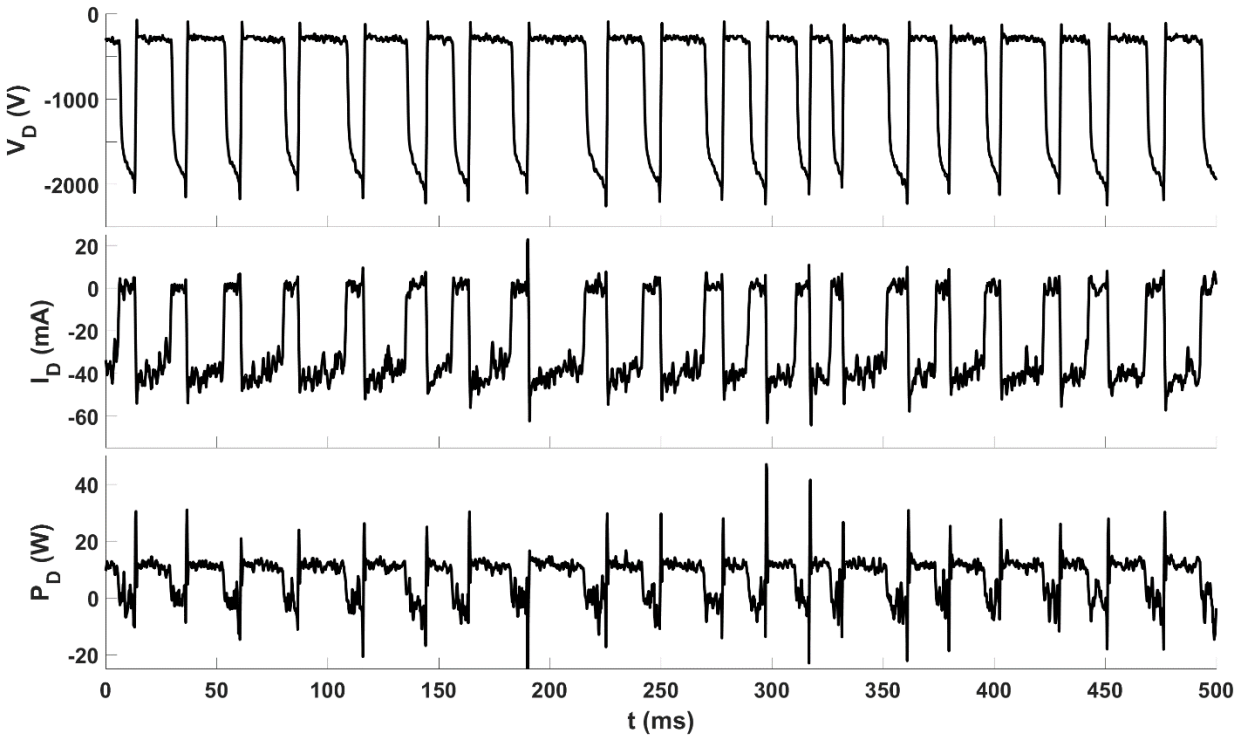

Figure 25. Discharge voltage (V_D), current (I_D) and power (P_D) signals for trial V_C = -300 V and Q = 8.8 SLPM.

To gain a better understanding of the train of events, the instantaneous V_D-I_D characteristics are shown in Figure 26. Looking at the entire signal (left), a typical arcing event can be broken down into various phases. The first one is the arc ignition or spark formation (identified with 1). During this short phase, the Cockcroft-Walton generator discharges at a voltage of around -2000 V, corresponding to a breakdown electric field magnitude of ~12 kV/cm. A seemingly instantaneous voltage drop is observed at which point the current-driver power supply takes over. With the setup used in this study, ~-200 V is the inter-electrode voltage at which the current-driver begins to take over. From this point on, the voltage increases slightly as the arc elongates and the discharge current decreases (phase 2). Figure 26 (right) shows a close-up view of the $V_D(t)$-$I_D(t)$ response during arcing (phase 2), clearly revealing the negative V_D-I_D characteristic of the arc. The zone with the high density of points (darker zone) shows the V_D-I_D region in which the arc operates for most of its lifetime. In this phase the arc is stable and elongates with time. As the arc elongates further (requiring a higher voltage) it reaches a point where there is not enough voltage to sustain

it. The start of the gliding arc extinction phase can be detected by the transition from a high density to a low density of data points. In Figure 26 (right), it can be seen that the arc extinguishes when $V_D \sim$ -240 V and $I_D \sim$ -30 mA. The fact that the gliding arc extinguishes before its voltage reaches V_C (-300 V in this trial) is due to the presence of the ballast resistance of 2 kΩ, which causes a ~60 V voltage drop. As the arc extinguishes, the discharge current rapidly drops to zero. The high voltage across the gap then rapidly builds up again (phase "3") when the 35-stage Cockcroft-Walton generator begins to cascade voltage through the capacitor bank. Since the AC power supply is set to 35 kHz, it takes ~1 ms to charge every capacitor in the set (1 stage charged per period of AC signal) which is seen as a drastic increase in voltage. The charging of the gap between the electrodes is then observed through an RC circuit with a time constant of ~2.5 ms (phase 4) before reaching the breakdown voltage and a new arc event repeating.

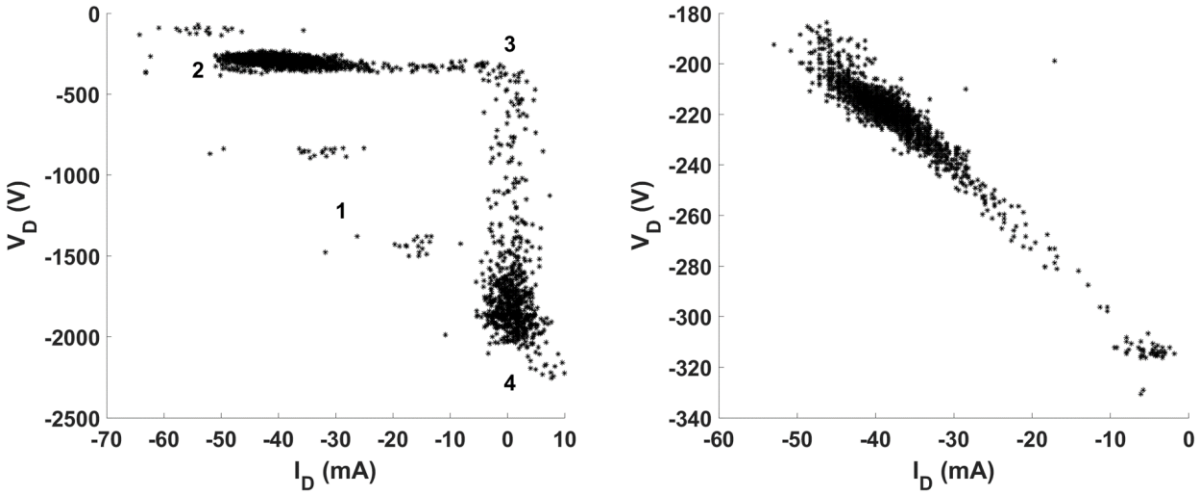

Figure 26. Discharge voltage-current characteristic of entire signal (left) and during the arcing phase (right) for the V_C = -300 V and Q = 8.8 SLPM trial.

As stated previously the average power and restrike frequency can be found at all operating conditions. Figure 27 displays the gliding arc average power (left) and restrike frequency (right) both plotted against the current driver output voltage and vortex gas flow rate. One observes that the average power increases with the applied current driver output voltage. The gliding arc average power decreases as the gas vortex flow rate is increased. This can be explained by referring to the

restrike frequency. As the gas flow rate increases, the restrike frequency also increases. At higher flow rates the drag force exerted on the arc column is much greater causing the arc to travel through the device quicker. This, and additional turbulence in the system cause the arcs to experience shorter lifetimes and a higher restrike frequency. Since the duration of phase 3 imposed by the Cockcroft-Walton generator is constant, at higher arcing frequencies the gliding arcs are active for proportionally shorter times, thus explaining the lower average power levels.

To understand the effect that the current driver output voltage has on the gliding arc restrike frequency, a deeper understanding of the power supply is required. As the current driver output voltage increases, the restrike frequency decreases until it reaches 0 Hz at any gas flow rate. When the current driver output voltage is set to 0 V, only the Cockcroft-Walton generator is active and it imposes a high restrike frequency (~1 kHz). Only repetitive spark ignition is observed, since there is not enough current to sustain a gliding arc. As the current driver output voltage is increased above a threshold of ~-200 V, gliding arcs start to form and the restrike frequency decreases. As the current driver output voltage is further increased, the restrike frequency continues to decrease until the arc becomes diffuse and immobile, with no more restrikes. This is true for each gas flow rate, however at higher flow rates a larger magnitude of voltage is required to anchor the arc. Increased turbulence makes it more difficult to stabilize the arc in this non-restrike mode. To the human eye the arc is fixed to one height in the device and appears as a flat disc. Thus, two different arc operation modes are observed: the desired restrike-gliding mode and the disc mode.

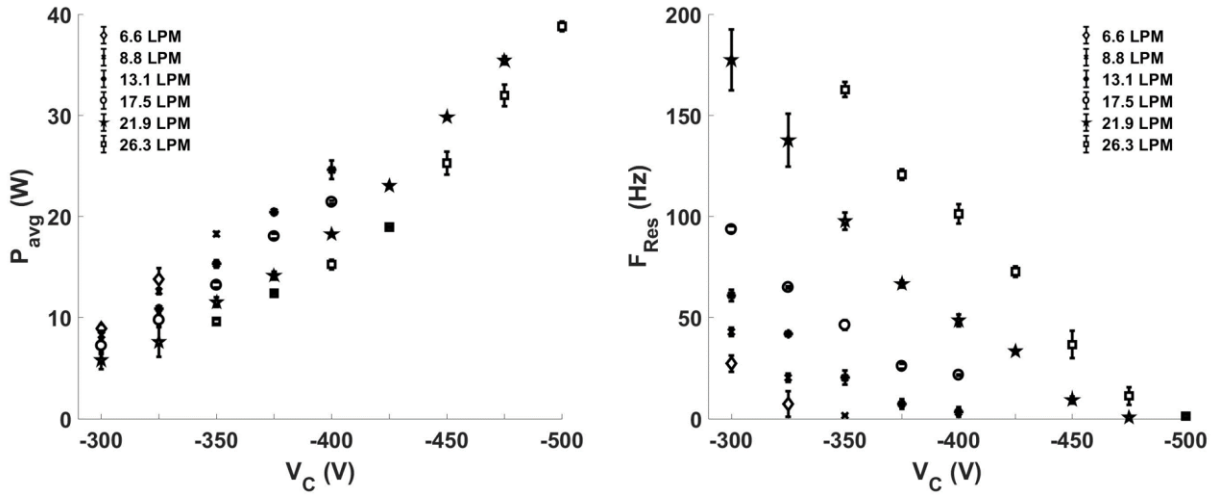

Figure 27. Average gliding arc discharge power (left) and restrike frequency (right) versus current driver output voltage and total argon flow rate.

4.2. Arc Motion Analysis

High-speed imaging was performed to understand how the applied current driver output voltage and total argon flow rate affect the rotating gliding arc dynamics. Figure 28 shows successive frames of an arcing event at a low current driver voltage, V_C = -325 V, and a moderate flow rate, Q = 13.1 SLPM. The dotted lines delineate the live conical cathode base and tip while the solid lines delineate the inside and outside diameters of the cylindrical grounded anode. These images acquired synchronously with the electrical signals act as the raw data for arc motion analysis. Consecutive frames are separated by 2.0 ms. At 19.5 ms, an arc is ignited at the shortest inter-electrode gap. As time progresses the arc elongates and rotates clockwise through the device (face-on view). A bright cathode spot is observed. The gliding arc displacement from the base to the top of the conical cathode can also be seen (up to 32.5 ms). Eventually, the arc reaches a length at which the power supply can no longer sustain it and it extinguishes. After some time (when the Cockcroft-Walton generator is recharging), a new arc ignites and the gliding arc process repeats itself.

Figure 28. High-speed imaging (2 ms between frames) of RGA in atmospheric pressure argon with V_C = -325 V and Q = 13.1 SLPM.

The disc operation mode is illustrated with Figure 29. In this mode, the arc slowly rotates and stays attached at a relatively constant height in the device. At high argon flow rates, the arc restrikes every ~500 ms while at low flow rates, the time lapse between restrikes can be of several seconds.

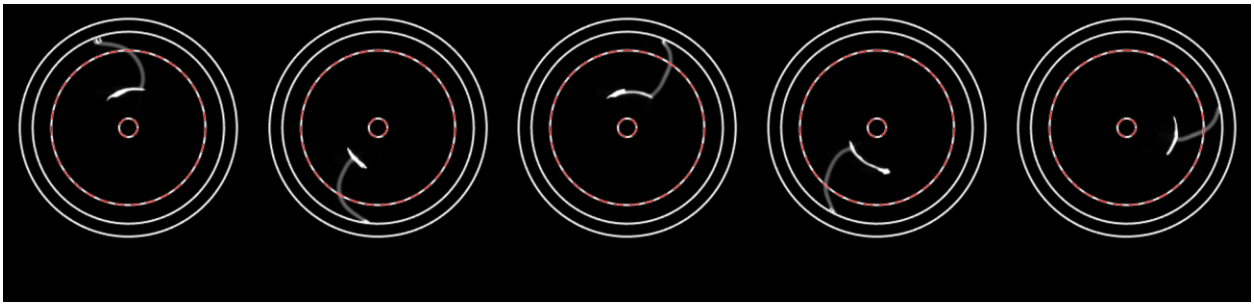

Figure 29. High-speed imaging (20 ms between frames) of RGA in disc mode with V_C = -325 V and Q = 6.6 SLPM.

We calculated several physical properties from the images, including the projected arc length (i.e. face-on view) and the height of the cathode spot (i.e. position w/r to the base of the cone). It must be noted that this length is the projected length as the camera is taking images face-on, thus any vertical displacement in the arc column is not detected. It is difficult to quantify the vertical displacement with the techniques used in this study, however it is easy to see where vertical displacement occurs. In the images, when there is vertical displacement a brighter node in the arc column is observed. This can be seen in various frames in Figure 28 where some locations in the arc column are brighter, indicating that there is some vertical displacement, albeit seeming small. When the arc column loops over itself as in the 32.5 ms frame of Figure 28, there is obviously some vertical displacement at the brighter node, however due to the camera looking face-on this cannot be quantified. With the knowledge of the slope of the conical cathode, the height of the cathode spot can be found using basic trigonometry. Since the arc is confined to below the tip of the conical cathode, the maximum height that can be obtained is 25.4 mm (i.e. the length of the cone).

Figure 30 displays the measured gliding arc discharge voltage compared with the calculated projected arc length and height of the cathode spot for various trials. Since the sustaining voltage of an arc is proportional to its length, both parameters are correlated as observed on the plots. It is interesting to note that the trial at the lowest total argon flow rate (left column) resulted in the disc mode, with corresponding images presented in Figure 29. The intermediate flow rate data (middle column) correspond to the images presented in Figure 28.

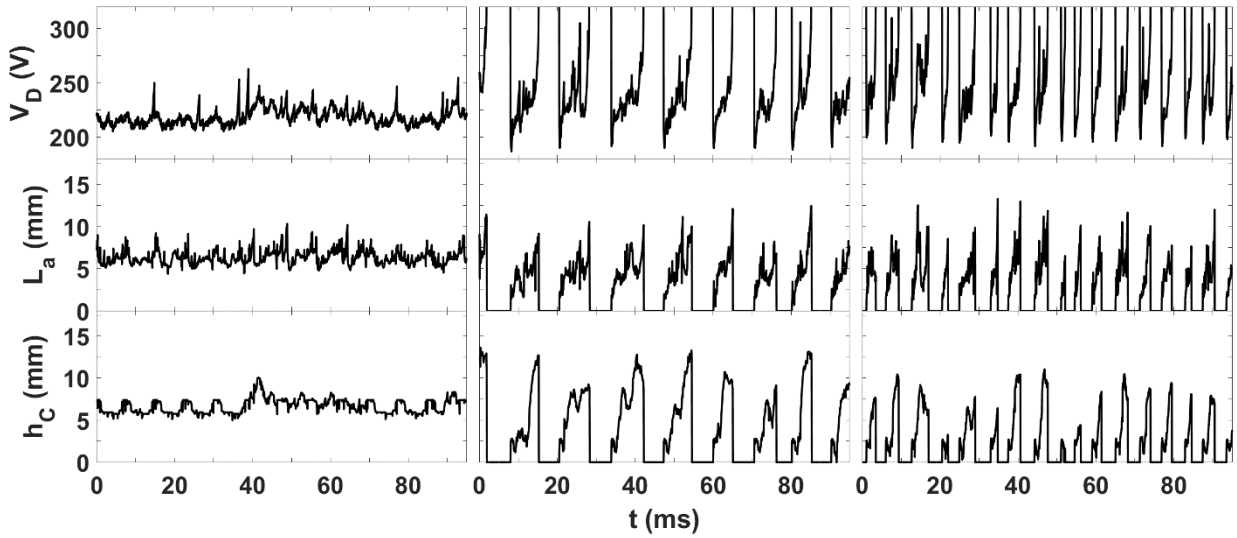

Figure 30. Measured gliding arc discharge voltage (top) displayed with calculated projected arc length (middle) and height of cathode spot (bottom) for three different trials. All trials at a constant V_C = -325 V and total flow rate, Q, of 6.6 (left), 13.1 (middle) and 21.9 (right) SLPM.

A comparison of the data across the different operating conditions is done by finding the average and maximum values of the projected arc length and height of the cathode spot, then performing a statistical analysis. The average and maximum arc length and cathode spot height are found from each individual full arc event. This means that in disc mode there is one continuous arc event considered, and in restrike mode there are only the number of events in that specific trial. Figure 31 shows the average and maximum projected arc lengths plotted against the applied current driver output voltage and total argon flow rate. An increase in voltage is associated with an increase in the projected arc length. The reason for this is that the current-driver power supply

kicks in at approximately -200 V, for every trial. Since an arc follows a negative V-I characteristic, at low current driver voltages (~-300 V) there is a small voltage range (~100 V) over which the arc can elongate. However, at high current driver voltages (~-500 V) there is a larger voltage range (~300 V) over which the arc can elongate, prior to extinction. The effect the total argon flow rate has on the gliding arc length is not quite as simple. At any given voltage, changing the flow rate has little effect on the average projected arc length. However, the maximum length seems to increase with an increase in flow rate. The disparity mainly arises as an artefact of the calculation method used. The average considers ignition, as well as the entire elongation phase. At low flow rates, the arc is alive longer (lower restrike frequency) allowing the average projected length to reach higher values. Conversely, at higher flow rates (high restrike frequency), the arc may reach a higher maximum length, but the quicker restrike frequency keeps the average length lower as the arc does not stay elongated to this extent for long durations. The reason the maximum projected arc length increases with respect to gas flow rate is due to the added drag force and increased turbulence. The arc tends to loop over itself more frequently at higher gas flow rates, an indicator of turbulence. This looping, along with an increased force on the arc column causing it to bow more allows the projected arc length to reach longer lengths. Another important observation from Figure 31 is that the data point for the lowest gas flow rate at any voltage represents the threshold above which the arc operates in the restrike mode. For this low threshold flow rate and below, the arc operates in the disc mode. Since the average and maximum values are found for each arc event, the rooted disc mode does not include the short lengths of ignition, giving rise to an overall longer length.

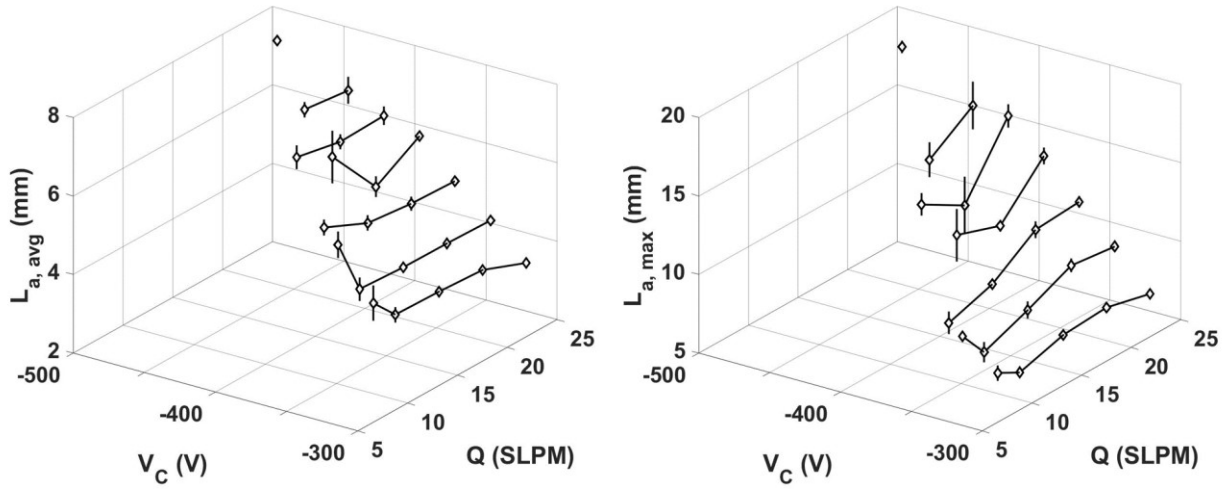

Figure 31. Average (left) and maximum (right) projected gliding arc length across all operating conditions. Note: Lines are not part of a model but rather used for ease of visualization.

The height of the cathode spot along the cone axis is compared across the operating conditions in a similar manner. Figure 32 shows the average and maximum height of the cathode spot plotted against the current driver output voltage and total argon flow rate. As the flow rate is increased a parabolic trend is observed for the cathode spot height. At low flow rates, there is not enough driving force to push the arcs far along the cone. Increasing the flow rate increases the drag force on the arc column, thus pushing the cathode spot downstream before reaching a maximum height. As the flow rate is increased further, a higher restrike frequency causes the average height of the cathode spot to stay relatively low. This parabolic trend is seen at the lower current driver voltages, but not at the higher values. The reason for this difference in behaviour is that the gliding arc at high current driver voltages operates in disc mode and does not begin to restrike until higher flow rates. Therefore, it is hypothesized that if the gas flow rate could be increased past ~25 SLPM a maximum will be reached, and the same parabolic trend would be observed. Unfortunately, the current setup does not allow such high flow rates, and this hypothesis cannot be tested. The maximum height the cathode spot can travel to corresponds to the length of the conical cathode which is 25.4 mm in the current setup. This maximum is only approached at high voltages and gas flow rates. An increase in current driver output voltage allows the arc to travel further through the device, by means of the cathode spot approaching the tip. This is likely due to the increased stabilization provided by the Lorentz force allowing the arcs to stay alive for a longer duration.

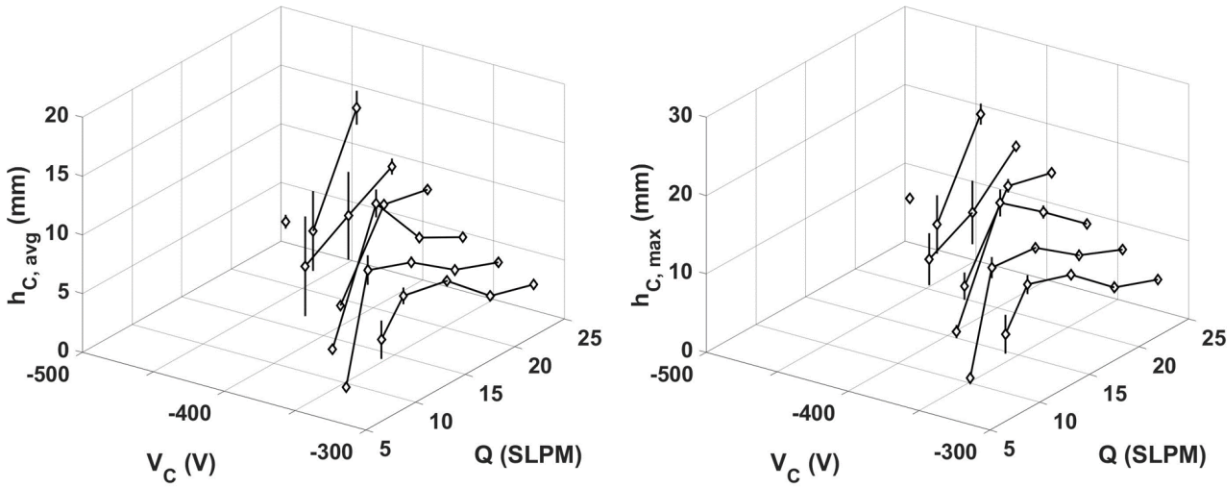

Figure 32. Average (left) and maximum (right) height of the cathode spot across all operating conditions. Note: Lines are not part of a model but rather used for ease of visualization.

To study the effect the magnetic field and flow field have on the arc column the frequency of arc rotation was found across all of the operating conditions. The two dominating forces acting on the arc column are the Lorentz force, induced by the magnetic field, and the drag force caused by the vortex flow field. The induced frequency of arc rotation can be found by applying equation 23.

Assuming an argon gas temperature in the $300<T<1000$ K range, the gas density range is $1.633>\rho>0.487$ kg/m^3 while this range is $2.23\text{x}10^{-5}<\mu<5.04\text{x}10^{-5}$ Pa.s for the dynamic viscosity. We estimated the Reynolds number in the discharge zone to be in the $10^2< Re = \rho u_{gas} D/\mu <10^4$ range. The gas velocity used to estimate the Reynolds was found by finding the ratio of the flow rate and the cross-sectional area in the discharge region. The diameter used in this calculation, D is the inside diameter of the anode (16.23 mm). The corresponding drag coefficient for a smooth cylinder is $1.1<C_d<1.3$ [35]. The arc column diameter was determined experimentally through image analysis and is typically in the $0.5<D_a<0.8$ mm range. As reported earlier, the magnetic field strength is expected to fall in the $0.043<B<0.122$ T range.

Figure 33 shows the results of an experiment conducted at no gas flow rate, in which the arc rotation solely due to the Lorentz force. To obtain this data set, the arcs were initiated with a

low argon flow, then this flow was set to zero causing the arcs to rotate in stagnant argon. Therefore, the gas velocity in equation 24 can be assumed to be zero to find a relationship between the arc rotating frequency and (magnitude of the) discharge current:

$$f_{Rot} = C_{arc}\sqrt{I_D} \tag{37}$$

where $C_{arc} = \frac{1}{\pi D}\sqrt{\frac{2B}{C_d \rho D_a}}$. Before applying Equation 37 a relationship between the current driver output voltage and discharge current is needed. This can be seen on Figure 33 (left), where a linear regression is applied. A good agreement is found with a R^2 very close to one and the fit is used as a means to interpolate the discharge current from the voltage, so equation 37 can be modelled. Figure 33 (right) shows the frequency of arc rotation plotted against the current driver output voltage for Q = 0 SLPM, along with model predictions using C_{arc} = 587.6 Hz/A$^{1/2}$, which value falls within the 141.6 < C_{arc} < 599.2 range obtained considering the lower and upper limits of all variables.

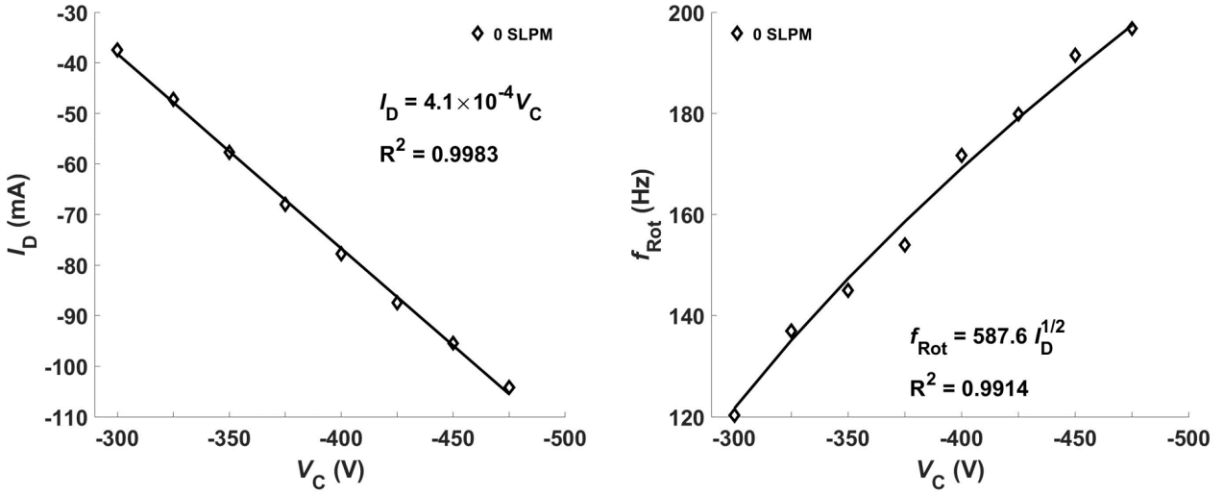

Figure 33. Measured and fitted average gliding arc discharge current (left) and frequency of arc rotation (right) versus current driver output voltage for Q = 0 SLPM.

Figure 34 (left) shows that the discharge current increases with an increase in current driver output voltage for all argon flow rates. Therefore, increasing the current driver output voltage leads to an increase of the gliding arc rotation frequency via the square root dependency (Figure 34 (right)). However, deviations from this trend become increasingly significant as the argon flow

rate is increased. This is likely because the flow rate has two effects on the overall frequency of arc rotation. The first is due to the effect the vortex gas flow rate has on the discharge current. The trend in Figure 34 (left) suggests that an increase in gas flow rate leads to a decrease of the average discharge current. The reason behind this is again due to the RGA having a higher restrike frequency at higher gas flow rates. Therefore, at higher gas flow rates, the relative contribution from the Lorentz force is lower. The second effect is directly related to the aerodynamic drag, in which a higher gas velocity forces the arc to rotate faster. This intricate relationship between the gas flow rate and magnetic field on frequency of arc rotation could explain the deviations observed at the higher gas flow rates.

Figure 34 (bottom) shows the effect of the direction of the external magnetic field on the gliding arc rotation frequency for a given current driver output voltage (V_C = -300 V) and over the range of argon flow rate. One observes that the gliding arc rotating frequency is directly proportional to the gas flow rate. This experimental observation confirms the simple model shown in Equation 23. There are two dominant forces acting on the arc column at any given time, the Lorentz force caused by the external magnetic field and the aerodynamic drag force caused by the gas flow. Reversing the direction of the external axial magnetic field by flipping around the ring magnets allows the Lorentz force to oppose the vortex flow (Figure 34 (bottom)). Here, we notice that an argon flow rate of ~8 SLPM is somewhat equivalent to the Lorentz force since both balance each other when acting in opposite direction. At gas flow rates lower than ~8 SLPM the Lorentz force dominates, and the arcs rotate in the opposite direction (negative frequency).

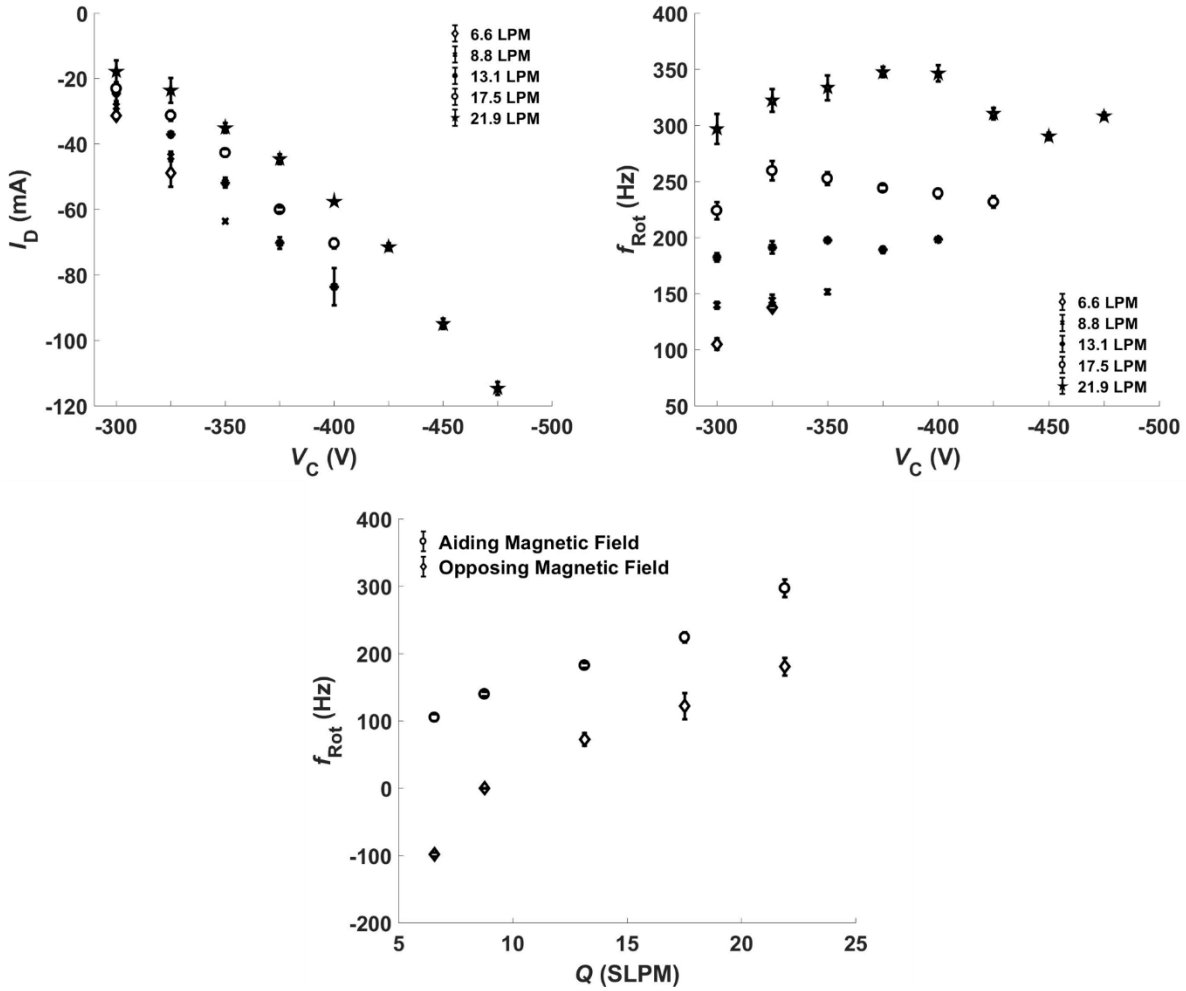

Figure 34. Gliding arc discharge current (left) and frequency of arc rotation (right) versus current driver voltage for various flow rates. Gliding arc rotation frequency at V_C = -300 V versus total argon flow rate and changing magnetic field direction (bottom). *Negative f_{Rot} means that the gliding arc rotates in the direction opposite to the one imposed by the aerodynamic drag.

Chapter 5. Conclusions

The dynamics of rotating gliding arcs established in atmospheric pressure argon between a conical cathode and a sleeve anode and powered by a homemade dual DC power supply was investigated by high-speed imaging and electrical diagnostics. The simple Cockcroft-Walton generator provided a stable train of -2000 V voltage pulses that repetitively ignited arcs which began gliding at a minimum sustaining voltage of ~-200 V. The gas vortex flow combined with the external static magnetic field provided stabilization of the gliding arcs. We observed that the average power of the gliding arcs increased with the applied DC voltage, but this power decreased as the gas vortex flow rate increased. We associated the later behavior to the increased restrike frequency, and the proportionally shorter individual arc lifetime. We also observed a mode transition from a gliding arc to a vertically stationary rotating arc attachment as the vortex gas flow rate was reduced to low values or when the applied voltage exceeded a threshold. In this operating regime the arc does not re-strike and if it does will re-ignite at the same vertical location.

We also found that flow rate had little effect on the length of the arc columns, but that the applied voltage showed a clear trend. As the arc elongates the arc voltage also increases. The maximum value that the arc voltage can reach is increased as the applied voltage is increased allowing the arc length to also increase. The arc was found to only approach the tip of the cathode at high applied voltages and flow rates. The square root dependency of the arc rotating frequency on the applied current predicted by a simplified model considering the gas vortex drag and Lorentz forces was confirmed with measurements, and the measured proportionality constant fell within the predicted limits. By reversing the direction of the external magnetic field, we demonstrated that the Lorentz force acting on the arc is equivalent to a ~8 SLPM vortex flow in the device. For lower flow rates, the magnetic force dominated.

Our observations delineate trade-offs for the further optimization of this device for gas processing. One would intuitively believe that increasing that vortex gas flow rate allows to elongate the arcs and to enhance the processing volume, but the accompanying increase in restrike frequency counteracts this action. Additional work should be dedicated to the optimization of the vortex gas injection angles, and to establish and sustain multiple simultaneous gliding arcs.

References

[1] Czernichwski, A. "Gliding arc. Applications to engineering and environmental control." *Pure & Applied Chemistry*., Vol. 66, No. 6, pp. 1301-1310 (1994).

[2] Gangoli, S. P., A. F. Gutsol, and A. A. Fridman. "A Non-Equilibrium Plasma Source: Magnetically Stabilized Gliding Arc Discharge: I. Design and Diagnostics." *Plasma Sources Science and Technology* 19, no. 6 (2010): 65003.

[3] Gangoli, S. P., A. F. Gutsol, and A. A. Fridman. "A Non-Equilibrium Plasma Source: Magnetically Stabilized Gliding Arc Discharge: II. Electrical Characterization." *Plasma Sources Science and Technology* 19, no. 6 (2010): 65004.

[4] Zhang, H., F. Zhu, X. Tu, Z. Bo, K. Cen, and X. Li. "Characteristics of Atmospheric Pressure Rotating Gliding Arc Plasmas." *Plasma Science and Technology* 18, no. 5 (2016): 473.

[5] Zhang, H., X. D. Li, Y. Q. Zhang, T. Chen, J. H. Yan, and C. M. Du. "Rotating Gliding Arc Codriven by Magnetic Field and Tangential Flow." *IEEE Transactions on Plasma Science* 40, no. 12 (December 2012): 3493–98.

[6] Ramakers, M., J. A. Medrano, G. Trenchev, F. Gallucci, and A. Bogaerts. "Revealing the Arc Dynamics in a Gliding Arc Plasmatron: A Better Insight to Improve CO_2 Conversion." *Plasma Sources Science and Technology* 26, no. 12 (2017): 125002.

[7] Wang, W., D. Mei, X. Tu, and A. Bogaerts. "Gliding Arc Plasma for CO2 Conversion: Better Insights by a Combined Experimental and Modelling Approach." *Chemical Engineering Journal* 330, no. Supplement C (December 15, 2017): 11–25.

[8] Hwang, N., J. Lee, D. H. Lee, and Y. H. Song. "Interactive Phenomena of a Rotating Arc and a Premixed CH4 Flame." *Plasma Chemistry and Plasma Processing* 32, no. 2 (January 14, 2012): 187–200.

[9] Wu, W. W., G. H. Ni, Q. F. Lin, Q. J. Guo, and Y. D. Meng. "Experimental Investigation of Premixed Methane Air Combustion Assisted by Alternating-Current Rotating Gliding Arc." *IEEE Transactions on Plasma Science* 43, no. 12 (December 2015): 3979–85.

[10] Locke P. R., M. Sato, P. Sunka, M. R. Hoffmann, and J. S. Chang, "Electrohydraulic discharge and nonthermal plasma for water treatment," *Industrial & Engineering Chemistry Research*, vol. 45, iss. 3 p. 882-905, 2006.

[11] Lu, S. Y., X. M. Sun, X. D. Li, J. H. Yan, and C. M. Du. "Decomposition of Toluene in a Rotating Glidarc Discharge Reactor." *IEEE Transactions on Plasma Science* 40, no. 9 (September 2012): 2151–56.

[12] Zhu, F., X. Li, H. Zhang, A. Wu, J. Yan, M. Ni, H. Zhang, and A. Buekens. "Destruction of Toluene by Rotating Gliding Arc Discharge." *Fuel* 176 (July 15, 2016): 78–85.

[13] Moreau, M., M. G. J. Feuilloley, N. Orange, and J. L. Brisset. “Lethal Effect of the Gliding Arc Discharges on Erwinia Spp.” *Journal of Applied Microbiology* 98, no. 5 (May 1, 2005): 1039–46.

[14] Fridman, A., S. Nester, L. A. Kennedy, A. Saveliev, and O. Mutaf-Yardimci. “Gliding Arc Gas Discharge.” *Progress in Energy and Combustion Science* 25, no. 2 (April 1999): 211–31.

[15] Czernichowski, A., H. Nassar, H. Ranaivosoloarimanana, A. A. Fridman, M. Simek, K. Musiol, and L. Dittrichova. (1996). Spectral and electrical diagnostics of gliding arc. *Acta Physica Polonica-Series A General Physics*, *89*(5), 595-604.

[16] Pellerin, S., J. M. Cormier, F. Richard, K. Musiol, and J. Chapelle. “A Spectroscopic Diagnostic Method Using UV OH Band Spectrum.” *Journal of Physics D: Applied Physics* 29, no. 3 (1996): 726.

[17] Chernets, I., G. Nirenberg, A. Fridman, A. Rabinovich. “Development of high-power plasma reformer and power supply for large scale applications”, *20th International Symposium on Plasma Chemistry*, July 24-29, 2011.

[18] Zhu, F., H. Zhang, X.-D. Li, A. Wu, J. Yan, M. Ni, and X. Tu. “Arc Dynamics of a Pulsed DC Nitrogen Rotating Gliding Arc Discharge.” *Journal of Physics D: Applied Physics*, 2018.

[19] Richard, F., J. M. Cormier, S. Pellerin, and J. Chapelle. “Physical Study of a Gliding Arc Discharge.” *Journal of Applied Physics* 79, no. 5 (March 1, 1996): 2245–50.

[20] Fridmann, A., L. Kennedy, *Plasma Physics and Engineering*, Taylor & Francis Group, 2011.

[21] Lieberman, M. A., A. J. Lichtenberg, *Principles of Plasma Discharges and Materials Processing, 2nd Edition*. John Wiley & Sons, Inc, 2005.

[22] Mutaf-Yardimci, O., A. V. Saveliev, A. A. Fridman, L. A. Kennedy. “Thermal and nonthermal regimes of gliding arc discharge in air flow.” *Journal of Applied Physics* 87, 1632 (2000).

[23] Baba, T., Y. Takeuchi, H. D. Stryczewska, and S. Aoqui. “Study of 6 Electrodes Gliding Arc Discharge Configuration.” *Przegląd Elektrotechniczny* R. 88, nr 6 (2012): 86–88.

[24] Nunnally, T., K. Gutsol, A. Rabinovich, A. Fridman, A. Gutsol, and A. Kemoun. “Dissociation of CO 2 in a Low Current Gliding Arc Plasmatron.” *Journal of Physics D: Applied Physics* 44, no. 27 (2011): 274009.

[25] Heijkers, S., and A. Bogaerts. “CO2 Conversion in a Gliding Arc Plasmatron: Elucidating the Chemistry through Kinetic Modeling.” *The Journal of Physical Chemistry C* 121, no. 41 (October 19, 2017): 22644–55.

[26] Trenchev, G., S. Kolev, W. Wang, M. Ramakers, and A. Bogaerts. “CO2 Conversion in a Gliding Arc Plasmatron: Multidimensional Modeling for Improved Efficiency.” *The Journal of Physical Chemistry C* 121, no. 44 (November 9, 2017): 24470–79.

[27] Cleiren, E., S. Heijkers, M. Ramakers, and A. Bogaerts. “Dry Reforming of Methane in a Gliding Arc Plasmatron: Towards a Better Understanding of the Plasma Chemistry.” *ChemSusChem* 10, no. 20 (October 23, 2017): 4025–36.

[28] Zhang, H., C. Du, A. Wu, Z. Bo, J. Yan, and X. Li. “Rotating Gliding Arc Assisted Methane Decomposition in Nitrogen for Hydrogen Production.” *International Journal of Hydrogen Energy* 39, no. 24 (August 13, 2014): 12620–35.

[29] Meek J. M., and J. D. Craggs. *Electrical Breakdown Of Gases*. Oxford At The Clarendon Press, 1953.

[30] Cockcroft, J. D., and E. T. S. Walton. "Experiments with High Velocity Positive Ions. (I) Further Developments in the Method of Obtaining High Velocity Positive Ions." *Proceedings of the Royal Society of London. Series A, Containing Papers of a Mathematical and Physical Character* 136, no. 830 (1932): 619-30.

[31] Ruzbehani, M. “A Comparative Study of Symmetrical Cockcroft-Walton Voltage Multipliers.” Research article. *Journal of Electrical and Computer Engineering*, 2017.

[32] Malik, M. A., K. H. Schoenbach, T. M. Abdel-Fattah, R. Heller, and C. Jiang. “Low Cost Compact Nanosecond Pulsed Plasma System for Environmental and Biomedical Applications.” *Plasma Chemistry and Plasma Processing* 37, no. 1 (January 1, 2017): 59–76.

[33] Horowitz, P., and W. Hill. *The Art of Electronics,* Third Edition. Cambridge University Press, 2015.

[34] Cormen, T. H., C. E. Leiserson, R. L. Rivest, and C. Stein. *Introduction to Algorithms*, Second Edition. MIT Press and McGraw-Hill, 2001.

[35] Munson, R. B., T. H. Okiishi, W. W. Huebsch, and A. P. Rothmayer. *Fundamentals of Fluid Mechanics* 7th Edition. John Wiley & Sons, Inc., 2013.